

**NAVAL POSTGRADUATE SCHOOL**  
**Monterey, California**

2

**AD-A272 426**



**DTIC**  
**ELECTE**  
**NOV 08 1993**  
**S B D**

**THESIS**

**The Use of Backscattered Electron Imaging Mode to Assess the  
Effect of Fine Dispersions on Development of Superplastic  
Microstructure in Al-Mg Alloys**

**by**

**Michael Thomas Coleman**

**June, 1993**

**Thesis Advisor:**

**Co-Advisor:**

**Terry R. McNelley**

**Peter N. Kalu**

**Approved for public release; distribution is unlimited.**

**93-27210**



**93 11 8 070**

# REPORT DOCUMENTATION PAGE

Form Approved  
OMB No. 0704-0188

Public reporting burden for this collection of information is estimated to average 1 hour per response, including the time for reviewing instructions, searching existing data sources, gathering and maintaining the data needed, and completing and reviewing the collection of information. Send comments regarding this burden estimate or any other aspect of this collection of information, including suggestions for reducing this burden, to Washington Headquarters Services, Directorate for Information Operations and Reports, 1215 Jefferson Davis Highway, Suite 1204, Arlington, VA 22202-4302 and to the Office of Management and Budget, Paperwork Reduction Project (0704-0188), Washington, DC 20503

1. AGENCY USE ONLY (Leave blank)		2. REPORT DATE June 1993		3. REPORT TYPE AND DATES COVERED Master's Thesis	
4. TITLE AND SUBTITLE The use of Backscattered Electron Imaging mode to assess the Effect of Fine Dispersions on the Development of Superplastic Microstructure in Al-Mg Alloys				5. FUNDING NUMBERS	
6. AUTHOR(S)  Michael Thomas Coleman					
7. PERFORMING ORGANIZATION NAME(S) AND ADDRESS(ES)  Naval Postgraduate School Monterey, CA 93943-5000				8. PERFORMING ORGANIZATION REPORT NUMBER	
9. SPONSORING / MONITORING AGENCY NAME(S) AND ADDRESS(ES)				10. SPONSORING / MONITORING AGENCY REPORT NUMBER	
11. SUPPLEMENTARY NOTES  The views expressed in this thesis are those of the author and do not reflect the official policy or position of the Department of Defense or the U.S. Government.					
12a. DISTRIBUTION / AVAILABILITY STATEMENT  Approved for public release; Distribution is unlimited				12b. DISTRIBUTION CODE	
13. ABSTRACT (Maximum 200 words)  Microstructural evolution during thermomechanical processing of several Al-Mg alloys was studied using backscattered orientation contrast imaging in the scanning electron microscope. The microstructural evolution in Al-8Mg-0.1Zr was characterized in three phases: (a) in the initial stages, precipitation occurred on prior boundaries and microbands were observed in the grain interiors; (b) during intermediate stages, higher order microbands were observed and precipitates formed throughout the microstructure on both lower- and higher-order microbands; (c) in the final stages, equiaxed regions appeared around larger particles suggesting particle stimulated nucleation of recrystallization. A higher Mg-content alloy (Al-10Mg-0.1Zr) was compared at two stages and seen to provide a greater volume fraction of similar sized precipitate. A finer recrystallized microstructure and greater superplastic response was observed in the Al-10Mg-0.1Zr alloy.					
14. SUBJECT TERMS  Backscattered Electron Imaging mode, Superplastic				15. NUMBER OF PAGES  76	
				16. PRICE CODE	
17. SECURITY CLASSIFICATION OF REPORT  Unclassified	18. SECURITY CLASSIFICATION OF THIS PAGE  Unclassified	19. SECURITY CLASSIFICATION OF ABSTRACT  Unclassified	20. LIMITATION OF ABSTRACT  SAR		

Approved for public release; distribution is unlimited.

The Use of Backscattered Electron Imaging Mode to Assess the  
Effect of Fine Dispersions on Development of Superplastic  
Microstructures in Al-Mg Alloys

by

Michael Thomas Coleman  
Lieutenant Commander, United States Navy  
B.A., Grambling State University

Submitted in partial fulfillment  
of the requirements for the degree of

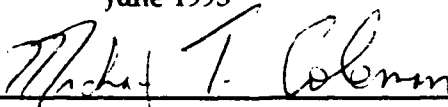
MASTER OF SCIENCE IN ENGINEERING SCIENCE

from the

NAVAL POSTGRADUATE SCHOOL

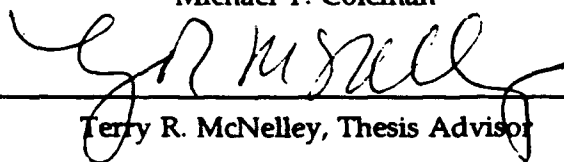
June 1993

Author:



Michael T. Coleman

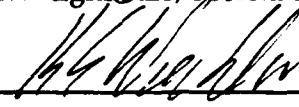
Approved by:



Terry R. McNelley, Thesis Advisor



John Neighbours, Second Reader



K. E. Woehler, Chairman  
Department of Physics

## ABSTRACT

Microstructural evolution during thermomechanical processing of several Al-Mg alloys was studied using backscattered orientation contrast imaging in the scanning electron microscope. The microstructural evolution in Al-8Mg-0.1Zr was characterized in 3 phases: (a) in initial stages, precipitation occurred on prior boundaries and microbands were observed in the grain interiors; (b) during intermediate stages, higher order microbands were observed and precipitates formed throughout the microstructure on both lower- and higher-order microbands; (c) in final stages, equiaxed regions appeared around larger particles suggesting particle stimulated nucleation of recrystallization. A higher Mg-content alloy (Al-10Mg-0.1Zr) was compared at two processing stages and seen to provide a greater volume fraction of similar sized precipitate. A finer recrystallized micro-structure and greater superplastic response was observed in the Al-10Mg-0.1Zr alloy.

DTIC QUALITY INSPECTED 5

<b>Accession For</b>	
NTIS GRA&I	<input checked="checked" type="checkbox"/>
DTIC TAB	<input type="checkbox"/>
Unannounced	<input type="checkbox"/>
Justification	
By	
Distribution/	
Availability Codes	
Dist	Avail and/or Special
A-1	

## TABLE OF CONTENTS

I. INTRODUCTION . . . . .	1
II. BACKGROUND . . . . .	4
A. INTRODUCTION . . . . .	4
B. SUPERPLASTICITY . . . . .	4
C. MICROSTRUCTURE . . . . .	6
D. ACHIEVING SUPERPLASTICITY THROUGH TMP . . . . .	7
E. IMAGING MODES . . . . .	9
F. BACKSCATTERED ELECTRON THEORY . . . . .	11
III. EXPERIMENTAL PROCEDURE . . . . .	14
A. MATERIALS . . . . .	14
B. THERMOMECHANICAL PROCESSING . . . . .	14
1. Solutioning Heat Treatment . . . . .	15
2. Forging . . . . .	16
3. Warm Rolling With IPAs . . . . .	16
C. TENSILE TESTING . . . . .	22
D. DATA REDUCTION . . . . .	23
E. SCANNING ELECTRON MICROSCOPY . . . . .	23
IV. RESULTS AND DISCUSSION . . . . .	24
A. MECHANICAL PROPERTIES . . . . .	25

B. ANALYSIS OF MICROSTRUCTURAL EVOLUTION DURING	
PROCESSING OF Al-8Mg-0.1Zr . . . . .	32
1. As-rolled condition, pass 3 ( $\epsilon=.254$ ): . . .	33
2. Annealed condition, after pass 3 ( $\epsilon=.254$ ): .	35
3. As-rolled condition, Pass 6 ( $\epsilon=0.845$ ): . . .	38
4. Annealed condition, after pass 6 ( $\epsilon=0.845$ ):	40
5. As-rolled condition, pass 8 ( $\epsilon=1.396$ ): . . .	43
6. Annealed condition after pass 8 ( $\epsilon=1.396$ ): .	45
7. As-rolled condition, pass 10 ( $\epsilon=1.949$ ): . .	48
8. Annealed condition after pass 10 ( $\epsilon=1.949$ ):	49
9. As-rolled condition, pass 12 ( $\epsilon=2.5$ ): . . .	50
10. Annealed condition after pass 12 ( $\epsilon=2.5$ ): .	51
C. COMPARISONS OF Al-10Mg-0.1Zr AND Al-8Mg-0.1Zr	
AFTER THE 3rd AND 12th PASSES . . . . .	52
1. As rolled condition, pass 3 ( $\epsilon=0.403$ ): . . .	52
2. Annealed condition after pass 3 ( $\epsilon=0.403$ ): .	55
3. As-rolled condition, pass 12 ( $\epsilon=2.6$ ): . . .	57
4. Annealed condition, after pass 12 ( $\epsilon=2.6$ ): .	59
V. CONCLUSIONS AND RECOMMENDATIONS . . . . .	61
A. THE FOLLOWING ARE THE MAIN CONCLUSIONS OF THIS	
WORK. . . . .	61
B. THE FOLLOWING ARE RECOMMENDED FOR FUTURE WORK .	62
LIST OF REFERENCES. . . . .	63
INITIAL DISTRIBUTION LIST . . . . .	65

## LIST OF FIGURES

Figure 2.1	Al-Mg-Zr phase showing TMP region . . . . .	8
Figure 2.2	The origin of Data signals in the SEM . . . . .	10
Figure 2.3	Relative energies of different electrons . . . . .	12
Figure 2.4	Emission of BSE as a function of atomic numbers . . . . .	13
Figure 3.1	TMP . . . . .	15
Figure 3.2	Tensile Test Specimen Design . . . . .	22
Figure 4.1	Strain rate coefficient for Al-10Mg-0.1Zr compared with previous work. . . . .	26
Figure 4.2	Strain rate coefficient $n$ for TMPs Al-10Mg-0.1Zr, Al-8Mg-0.1Zr and Al-8Mg . . . . .	28
Figure 4.3	Ductility vs strain rate for TMPs Al-10Mg-0.1Zr, Al-8Mg-0.1Zr & Al-8Mg . . . . .	29
Figure 4.4	Ductility vs strain rate for TMP Al-10Mg-0.1Zr (compared to previous work) . . . . .	30
Figure 4.5	Backscattered electron micrograph showing Al-10Mg-0.1Zr following pass 3 (as-rolled). . . . .	34
Figure 4.6 a & b	Backscattered electron micrographs showing Al-8Mg-0.1Zr following pass 3; after 25 minutes annealing at 300°C. . . . .	36
Figure 4.6	Backscattered electron micrograph showing Al-8Mg-0.1Zr following pass 3; . . . . .	37

<b>Figure 4.7</b>	<b>Backscattered electron micrograph of</b>	
	<b>Al-8Mg-0.1Zr following pass 6; (as-rolled).</b>	<b>39</b>
<b>Figure 4.8.a</b>	<b>Backscattered electron micrograph of</b>	
	<b>Al-8Mg-0.1Zr following pass 6; after 25 minutes</b>	
	<b>of annealing b) a section of 4.8.a at a higher</b>	
	<b>magnification</b>	<b>41</b>
<b>Figure 4.8.c</b>	<b>Backscattered electron micrograph of</b>	
	<b>Al-8Mg-0.1Zr following pass 6; depicts a section</b>	
	<b>of 4.8.a at higher magnification.</b>	<b>42</b>
<b>Figure 4.9.a</b>	<b>Backscattered electron micrograph showing</b>	
	<b>Al-8Mg-0.1Zr following pass 8; (as-rolled).</b>	<b>43</b>
<b>Figure 4.9 b)</b>	<b>Backscattered electron micrograph of</b>	
	<b>Al-8Mg-0.1Zr following pass 8; (as-rolled)</b>	
	<b>c) depicts region of 4.9.b at higher magnification</b>	<b>44</b>
<b>Figure 4.10 a)</b>	<b>Backscattered electron micrograph showing</b>	
	<b>Al-8Mg-0.1Zr following pass 8; after 25 minutes of</b>	
	<b>annealing at 300°C. b) at higher magnification.</b>	<b>46</b>
<b>Figure 4.10.c</b>	<b>Backscattered electron micrograph of</b>	
	<b>Al-8Mg-0.1Zr following pass 8; after 25 minutes of</b>	
	<b>annealing; region of very little precipitation.</b>	<b>47</b>
<b>Figure 4.11</b>	<b>Backscattered electron micrograph of</b>	
	<b>Al-8Mg-0.1Zr following pass 10; (as-rolled).</b>	<b>48</b>
<b>Figure 4.12</b>	<b>Backscattered electron micrograph showing</b>	
	<b>Al-8Mg-0.1Zr following pass 10; after 25 minutes</b>	
	<b>of annealing at 300°C.</b>	<b>49</b>



<b>Figure 4.13</b>	<b>Backscattered electron micrograph of</b>	
	<b>Al-8Mg-0.1Zr following pass 12; (as-rolled).</b>	<b>50</b>
<b>Figure 4.14</b>	<b>Backscattered electron micrograph showing</b>	
	<b>Al-8Mg-0.1Zr following pass 12; after 25 minutes of</b>	
	<b>annealing at 300°C.</b>	<b>51</b>
<b>Figure 4.15.a</b>	<b>Backscattered electron micrographs showing</b>	
	<b>Al-10Mg-0.1Zr following pass 3; (as-rolled).</b>	<b>53</b>
<b>Figure 4.15.b</b>	<b>Backscattered electron micrograph of</b>	
	<b>Al-10Mg-0.1Zr following pass 3; (as-rolled)</b>	<b>54</b>
<b>Figure 4.16</b>	<b>Backscattered electron micrographs showing</b>	
	<b>Al-10Mg-0.1Zr following pass 3; after 25 minutes of</b>	
	<b>annealing at 300°C.</b>	<b>56</b>
<b>Figure 4.17</b>	<b>Backscattered electron micrographs of</b>	
	<b>Al-10Mg-0.1Zr following pass 12; (as-rolled)</b>	<b>58</b>
<b>Figure 4.18</b>	<b>Backscattered electron micrograph of</b>	
	<b>Al-10Mg-0.1Zr following pass 12; after 25 minutes</b>	
	<b>of annealing at 300°C.</b>	<b>60</b>

### **ACKNOWLEDGMENTS**

I would like to express my sincere gratitude to Professor Terry McNelley for providing his insightful guidance and direction in this research endeavor. I wish to thank Dr. Peter Kalu for encouraging me to pursue research in this area and for his technical support and professional guidance. Also, I wish to thank Captain Bruce Woodruff for encouraging me and giving me the time off necessary to complete this research. A special thanks to my wife Priscilla, and my children, Michael Jr. and Dana Michelle, for their patience, understanding and encouragement during my studies and efforts to complete this endeavor.

## I. INTRODUCTION

Metallic materials are especially useful because they combine strength and the capacity to deform plastically. Some metals exhibit an exceptional ability to elongate under certain conditions and are called superplastic. Superplasticity is the ability of a metallic material to elongate in excess of 200% in tension [Ref.1]. Careful control of temperature, strain rate and microstructure is required in order to achieve superplasticity [Ref.2]. Under appropriate conditions of temperature and strain rate, superplastic metals exhibit a low resistance to plastic flow and display remarkable formability. Complex shapes can be formed from single pieces of these metals using only gas pressure and simple dies and with minimum expenditure of energy. Such capabilities have resulted in important cost savings and performance improvements for both military and industrial applications. For example, Rockwell International superplastically formed a single piece of a Ti alloy to replace a B-1 aircraft component which had previously involved the forming of eight separate pieces of the same alloy joined together with 96 fasteners (estimated cost savings of 55% and weight savings of 33%) [Ref.3]. Other alloys including nickel-based materials and ultrahigh-carbon steels have been used in equally impressive ways with equally impressive

savings [Ref.3]. Also, Al-based alloys are also being commercially developed for superplastic forming applications [Ref.3].

Research on processing of Al-Mg alloys at the Naval Post Graduate school began in 1976 and first considered very high Mg content (up to 18 weight percent) alloys [Refs.4,5]. Later efforts were directed at processing of alloys containing 7-10 weight percent Mg [Refs.6,7] and characterization of microstructure by optical [Ref.8] and transmission electron microscopy (TEM) [Ref.9] methods. Subsequent refinements of the thermomechanical processing (TMP) have lead to continued improvement and, in recent work [Ref.10], superplastic ductility of 1100% in Al-10Mg-0.1Zr alloy (composition in weight percent) has been attained.

Microscopy studies of these superplastic materials have been concerned mainly with the fully processed materials. Only one detailed, systematic study has been conducted [Ref.11] at earlier stages in the processing. In all cases, the relevant features of microstructure are too fine for investigation using optical microscopy methods. Recent developments in this laboratory have enabled the microstructure of these alloys to be studied using the Back Scattered Imaging (BSI) mode in a Scanning Electron Microscope (SEM). Metallographic polishing techniques have been developed which allow distinct orientation contrast to be revealed under appropriate imaging conditions in as-polished

samples. Use of this SEM technique enables grain and subgrain structures to be imaged on bulk, as-polished specimens, with a resolution intermediate between optical and TEM methods. The advantage relative to TEM is that the whole of the specimen cross section can be studied, which is essential if isolated events or long range variations in microstructure are to be detected.

In this research, the primary focus was to study the microstructure at various steps of the TMP, using the BSI orientation contrast mode of the SEM in order to provide a better understanding of the evolution of microstructure leading to superplasticity.

## II. BACKGROUND

### A. INTRODUCTION

There is considerable military and industrial interest in the processing and properties of Al-Mg alloys. Aluminum ranks second only to iron and steel in terms of volume and weight used industrially, with Al-Mg alloys making up nearly half the total production tonnage of all Al-based materials [Ref.12]. Also, Al alloys have high potential strength to weight ratios while maintaining corrosion resistance, machinability, ductility and toughness [Ref.13]. Superplasticity in Al-alloys is of interest because superplastic forming may result in significant weight reductions and fabrication cost savings [Ref.13].

This chapter will provide further background on superplasticity, its microstructural prerequisites and the necessary TMP to achieve it in Al-Mg alloys. Additionally, the SEM imaging modes used in this area of research will be discussed.

### B. SUPERPLASTICITY

From the viewpoint of applied mechanics, the highly ductile nature of superplastic materials is the result of their high strain-rate sensitivity. The relationship between

the flow stress and strain rate for many materials is given by:

$$\sigma = K\dot{\epsilon}^m \quad (2.1)$$

where,  $\sigma$  is the flow stress,  $\dot{\epsilon}$  is the strain rate and  $K$  and  $m$  are material constants [Ref.3]. The coefficient  $m$  is often termed the strain rate sensitivity. It has been shown experimentally that the elongation to failure increases as  $m$  increases [Ref.3]. The higher the value of  $m$ , the greater is the suppression of localized necking. This, in turn, allows for greater uniform extension and thus higher elongation. The value of  $m$  can be determined from double logarithmic plots of flow stress vs. strain rate by applying the relation:

$$m = \Delta \ln \sigma / \Delta \ln \dot{\epsilon} \quad (2.2)$$

Data for many materials suggest a sigmoidal relationship between stress and strain rate. Then, the maximum ductility is seen to correspond to the strain rate of maximum  $m$  value [Ref.3]. Most superplastic metals exhibit a maximum value of  $m = 0.5$ .

The superplastic response is very sensitivity to grain size. The dependence of strain rate on grain size (at constant stress and temperature) has been shown to be either  $\dot{\epsilon} \propto d^{-2}$  or  $\dot{\epsilon} \propto d^{-3}$  [Ref.3]. Therefore, at a given stress the

strain rate invariably increases with a decrease in grain size, i.e., the material weakens as grain size decreases.

### C. MICROSTRUCTURE

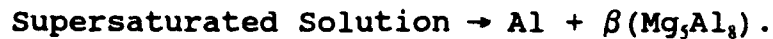
Along with grain size, additional microstructural features important for the development of superplastic response include: (a) the amount, strength, size and distribution of second phases; (b) the nature of the grain boundaries; and (c) the grain shape [Ref.3].

A fine grain size has long been recognized as a necessary prerequisite for superplasticity. Typically, a grain size less than 10  $\mu\text{m}$  is required and a smaller grain size, 1-2 $\mu\text{m}$  is necessary to facilitate superplasticity at lower temperatures. The addition of Zr to Al-based alloys provides as-cast grain refinement and hence assists in providing homogeneity to the starting ingot. Additionally, the  $\text{Al}_3\text{Zr}$  intermetallic which forms by precipitation in the solid state is very fine and very slow to coarsen. Hence, the addition of Zr is useful for achieving microstructural stability at superplastic forming temperatures [Refs.14,15]. The presence of Zr in solid solutions may also aid in grain refinement.

In order to maintain a fine grain size at the superplastic forming temperature the presence of a second phase at the matrix grain boundaries is required. The addition of Mg to Al-alloys results in a lighter, but stronger material. Most of the strength from the addition of Mg to these alloys is due



to solid solution strengthening. However when the solubility of Mg is exceeded, a second phase is formed. This formation may be described by [Ref.16]



A sufficient quantity of the second-phase  $\beta$  precipitates distributed uniformly as fine particles during processing facilitates the superplastic response by providing a refined, stable grain structure [Ref.3].

Grain boundary sliding is the predominant mode of deformation during superplastic forming [Ref.3]. Low-angle grain boundaries do not slide under shearing stresses. In order to facilitate grain boundary sliding, there must be a sufficient misorientation angle between grains. Thus, structures containing low-angle grain boundaries are not superplastic. A superplastic response can be attained by altering the TMP to provide high-angle rather than low-angle boundaries [Ref.3]. In order to facilitate the extensive grain boundary sliding characteristic of superplasticity, grains should also be equiaxed in shape [Ref.3].

#### **D. ACHIEVING SUPERPLASTICITY THROUGH TMP**

TMP is used in order to develop the microstructure necessary for achieving superplasticity in Al alloys. In Al-Mg alloys of sufficiently high Mg content, a dispersed second phase is produced through a solutioning treatment above the

solvus followed subsequently by warm working below the solvus temperature (Figure 2.1). With a sequence of warm rolling passes and interpass anneals (IPAs), dislocation generation

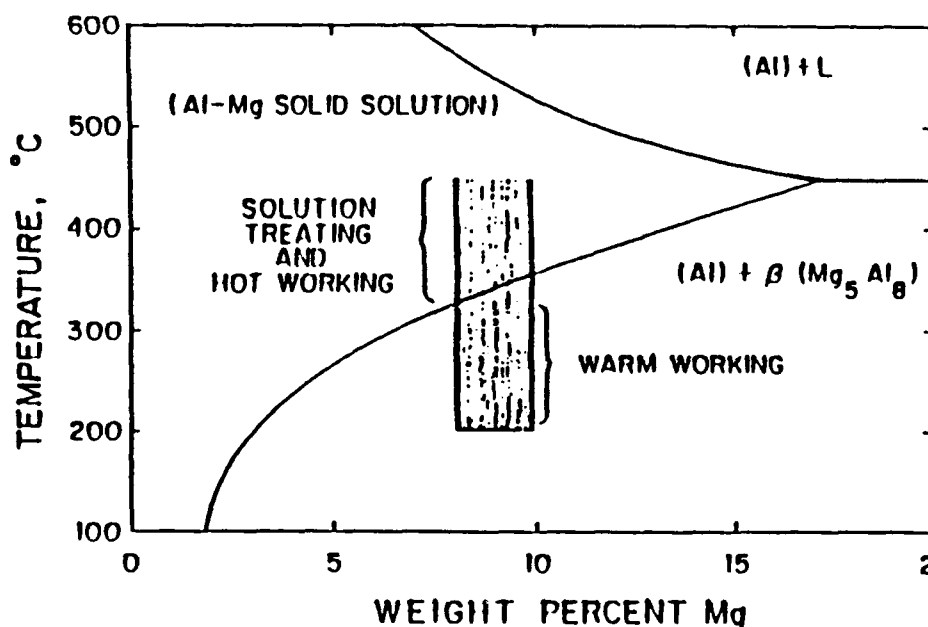


Figure 2.1 Al-Mg-Zr phase showing TMP region [Ref.8].

and dynamic recovery alternate with static recovery and second-phase precipitation [Ref.17]. It has been proposed that a prolonged IPA time (30 minutes) may result in the development of particle-stabilized subgrain boundaries of moderate misorientations. Subsequently, it has been

recognized that  $\beta$ -phase particles become sites for particle-stimulated nucleation (PSN) of recrystallization upon annealing after the final rolling passes [Ref.18]. This microstructure transformation is not fully understood.

#### **E. IMAGING MODES**

Attempts to study the evolution of microstructure during processing by use of TEM have been hindered by several factors including imaging problems due to high dislocation densities in the as-rolled condition after a rolling pass. However, TEM has been effective for evaluating grain morphology and grain boundary misorientation when samples were first subjected to a brief anneal. The use of TEM methods alone may result in the overlooking of isolated events in microstructural evolution which are more apparent in the examination of bulk material. The customary method for such studies of bulk material has been by optical metallography. Standard techniques have been unsuccessful when applied to this material due to the large volume fraction of second-phase precipitate particles and their effect on etching response. The SEM provides a useful alternative for samples which are difficult to etch, since grain structures can be examined from electropolished surfaces. Here, we use the backscattered imaging technique in conjunction with methods to enhance orientation contrast and thereby address the evolution of microstructure [Ref.18].

Imaging in the SEM results from interactions of an incident electron beam with atoms of a target sample. The image obtained is a result of either elastic or inelastic scattering collisions of the beam electrons with the sample. Figure 2.2 indicates how the SEM may utilize a number of different signals to produce an image from a sample.

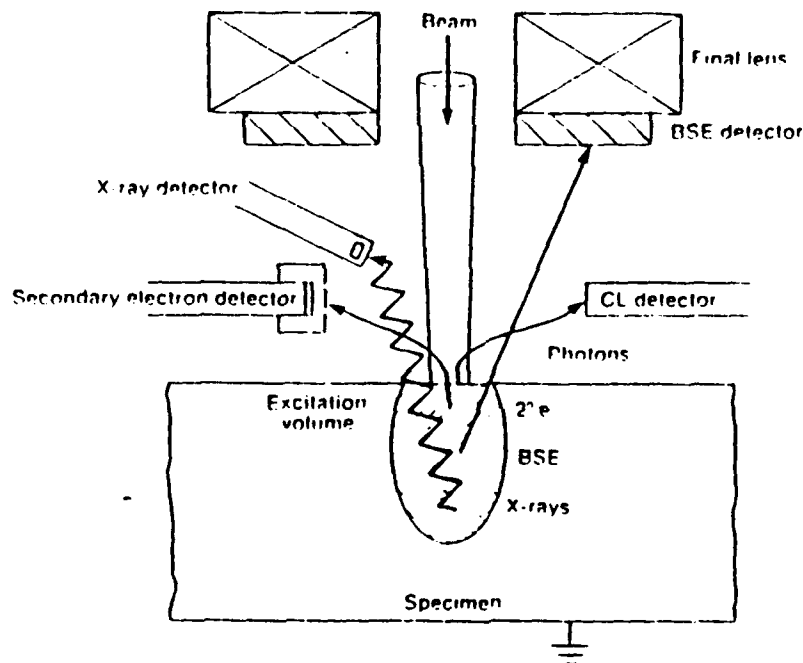


**Figure 2:2 The origin of Data signals in the SEM [Ref.15].**

Secondary electrons are low energy electrons ( $\leq 50\text{eV}$ ) emitted as a result of inelastic collisions between the beam electrons and the specimen electrons, [Ref.19]. Topographical

contrast resulting from the surface features of the primary specimen is the essential data provided by secondary imaging with this technique.

In Back Scattered Electron (BSE) imaging the contrast arises from both orientation effects and atomic number differences. Orientation contrast is seen because backscattered intensity is a function of the incident angle of the electron beam with respect to the crystal planes. Atomic number contrast arises because heavier atoms (higher atomic number) are more efficient at scattering electrons. Thus it is possible to use BSEs to detect composition differences if the differences result from a change in the mean atomic weight with position. In fact, this technique is sensitive enough to detect regions differing by less than one atomic mass unit (in mean atomic weight) [Ref.20]. Therefore, the atomic number contrast can provide both topographic and compositional specimen data.

#### **F. BACKSCATTERED ELECTRON THEORY**

An elastic interaction occurs when an incident electron interacts with the nucleus of a sample atom and is reflected back with very little loss energy loss ( $\approx 20\%$  below the energy compared to the incident beam energy, as shown in Figure 2.3), and also a small angular deflection. The reflected electron is referred to as a backscattered electron because the same electron enters the sample and rebounds.

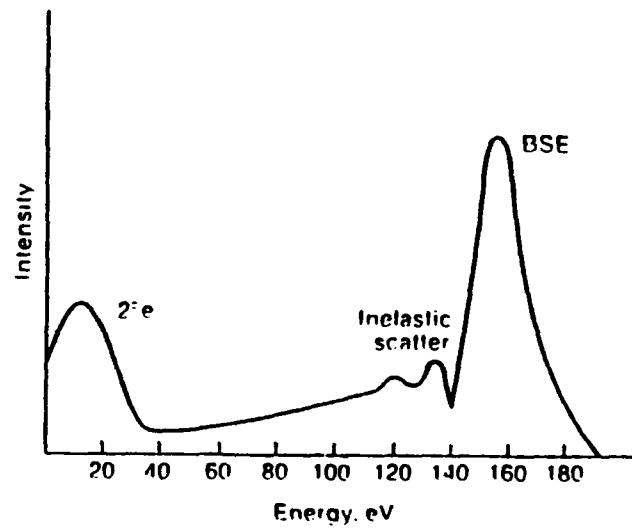


**Figure 2.3 The relative energies of different electrons [Ref.15].**

The likelihood of backscattering an incident electron is a function of the sample's mean atomic weight ( $Z$ ). High- $Z$

metals provide more elastic interactions than the lower-Z metals because of a higher density of nuclei which scatter more strongly. Figure 2.4 is an illustration of how  $\eta$ , the backscattering coefficient, increases as a function of Z [Ref.15].

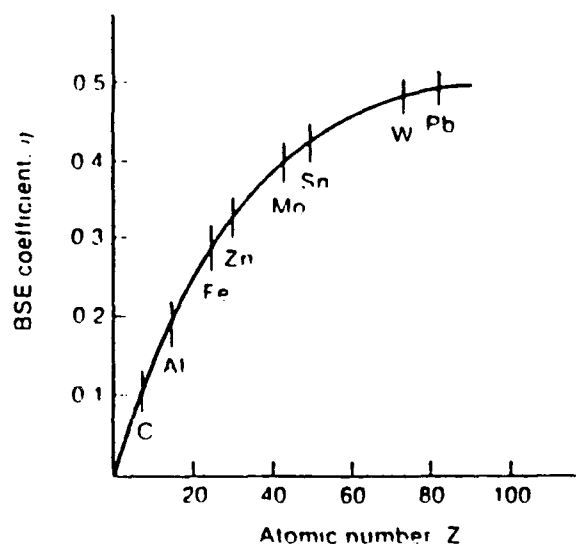


Figure 2.4 The emission of BSE as a function of atomic numbers [Ref.15].

### III. EXPERIMENTAL PROCEDURE

The experimental procedures for processing and mechanical testing described in parts A through D duplicate with minor modifications those of Gorsuch [Ref.10]. The SEM methods (Part E) were developed specifically for this work.

#### A. MATERIALS

Three Al-Mg alloys with casting numbers S572826 (Al-9.89Mg-0.09Zr), S572823 (Al-8.11Mg-0.12Zr), and S572821 (Al-8.2Mg) were examined in this research. Compositions are given in weight percent. They were provided by the ALCOA Technical Center, Alcoa center, Pennsylvania, as direct-chill cast ingots 150mm in diameter. Billets for subsequent TMP were prepared with dimensions of 31.8mm x 31.8mm x 95.4mm. The long dimensions of the billets was parallel to the ingot casting direction.

#### B. THERMOMECHANICAL PROCESSING

The TMP consisted of three parts (Figure 3.1): (a) solutioning heat treatment, (b) hot working via forging, (c) warm rolling with IPAs to maintain isothermal conditions.



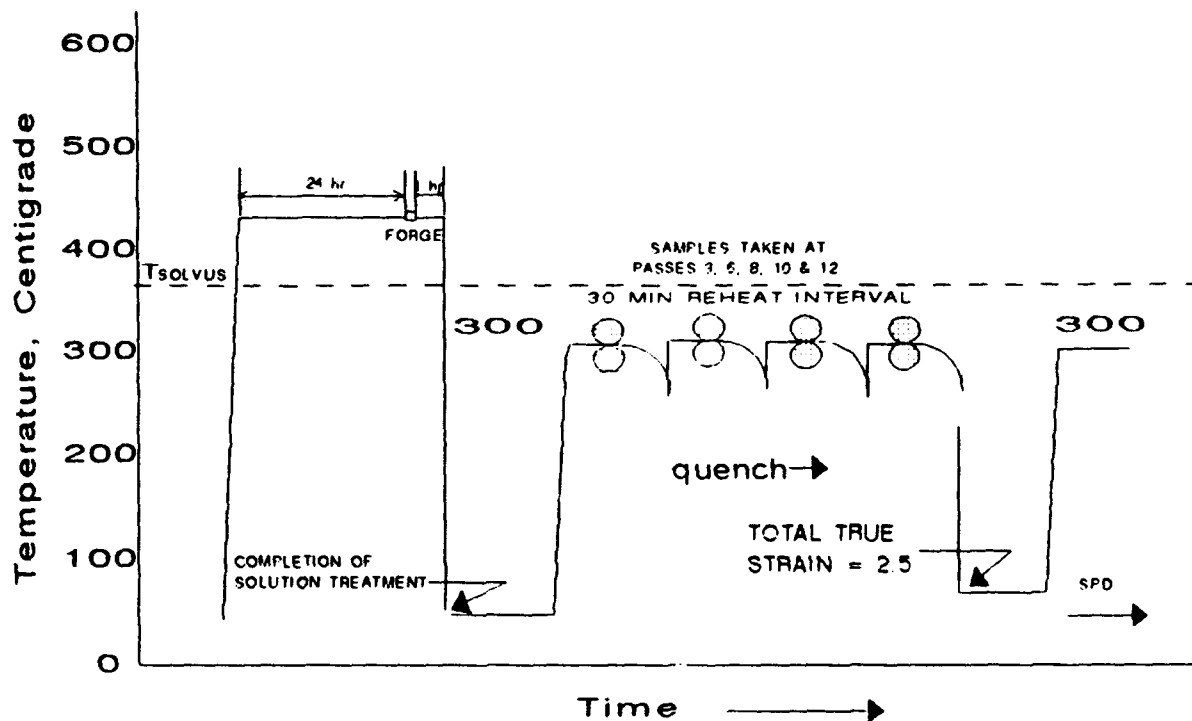


**Figure 3.1 TMP**

### **1. Solutioning Heat Treatment**

Solution treatment for homogenization for 6 hours at 440°C followed by 18 hours at 500°C was conducted utilizing a Lindberg type B-6 Heavy Duty furnace.

## **2. Forging**

Upset forging of the billets was performed at 440°C using a Baldwin-Tate-Emery testing machine equipped with heated platens. The billet was upset along the longitudinal axis to a 3.75:1 reduction resulting in a final thickness of approximately 1.0 inch (25.4 mm). The forged billets were replaced in the 440°C furnace for one hour and then quenched in oil. The billets were sectioned to "square" the sides in order to reduce the possibility of edge cracking during rolling.

The forged billets were placed in a Blue M furnace, model 8655-3, for 30 minutes of initial heating. The IPA time represented the time the material was in the furnace and did not include the time (less than one minute) to transfer the billet to the rolling mill and return to the furnace. A large steel plate was fitted to the bottom of the furnace to act as a heat sink in order to aid in maintaining a stable annealing temperature.

## **3. Warm Rolling With IPAs**

The final part of the TMP was performed utilizing 12 rolling passes to achieve a true strain  $\epsilon = 2.5$  while the IPA time was maintained at 30 minutes.

The billets were rolled using a Fenn Laboratory Rolling Mill following the reduction schedules as shown in Tables 3.1-3.3. The reduction schedules were developed from

that used by Gorsuch [Ref.10] by modifications to achieve an increasing or constant strain per pass and a continuously increasing strain rate on successive passes. Mill gap represents the actual separation between the rollers (inches). A set of stainless steel gauges were machined to dimensions corresponding to the calculated values for the mill gap settings shown in the tables and were used to accurately set the roller separations prior to each pass. The columns  $t_i$  and  $t_f$  represent the measured thickness of the specimens before and after each rolling pass, respectively. The column labeled  $\Delta t = (t_i - t_f)$  gives the reduction in the thickness of the specimens after each pass. The mill deflections were determined by subtracting the actual mill gap setting prior to rolling from value  $t_f$  after each pass. The column  $e_i$  represents the engineering strain for each pass calculated by:

$$e_i = (t_f - t_i) / t_i = \Delta t / t_i \quad (4.1)$$

and  $\epsilon_i$  represents the true strain for each pass, given by:

$$\epsilon_i = \ln(t_i / t_f) \quad (4.2)$$

Finally,  $\Sigma \epsilon_i$  represents the cumulative true strain following each rolling pass. As shown in Tables 3.1-3.3, the actual strain per rolling pass generally increased with each successive rolling/annealing cycle. After rolling passes 3, 6, 8, 10, and 12, small samples of the material were sectioned using a band saw, followed by a water quench to room temperature. The quenched samples were then further cut in half, with one of the halves being annealed for 25 minutes at 300°C. This represented the IPA following the pass in question.

TABLE 3.1: ROLLING SCHEDULE FOR Al-10Mg-0.1Zr

PASS	MILL GAP (in)	$t_i$ (in)	$t_f$ (in)	$\Delta t$ (in)	MILL DEFLECTION	$e_i$	$e_f$	$\Sigma e_i$
1	0.900	1.065	0.941	0.124	0.041	.116	0.124	0.124
2	0.790	0.941	0.823	0.118	0.033	.125	0.134	0.258
3	0.680	0.823	0.712	0.111	0.032	.135	0.145	0.403
4	0.570	0.712	0.604	0.108	0.034	.152	0.165	0.567
5	0.460	0.604	0.500	0.104	0.040	.172	0.189	0.756
6	0.350	0.500	0.383	0.117	0.033	.234	0.267	1.023
7	0.265	0.383	0.299	0.084	0.034	.219	0.248	1.270
8	0.195	0.299	0.234	0.065	0.039	.217	0.245	1.515
9	0.140	0.234	0.174	0.060	0.034	.256	0.296	1.812
10	0.100	0.174	0.138	0.036	0.038	.207	0.232	2.043
11	0.070	0.138	0.104	0.034	0.034	.246	0.283	2.326
12	0.047	0.104	0.079	0.025	0.032	.240	0.275	2.601

TABLE 3.2: ROLLING SCHEDULE FOR Al-8Mg-0.1Zr

PASS	MILL GAP (in)	$t_i$ (in)	$t_f$ (in)	$\Delta t$ (in)	MILL DEFLECTION	$e_i$	$\epsilon_i$	$\Sigma \epsilon_i$
1	0.900	--	--	--	--	--	--	--
2	0.790	0.913	0.818	.095	0.038	.104	.110	.110
3	0.680	0.818	0.708	.110	0.028	.134	.144	.254
4	0.570	0.708	0.600	.108	0.030	.153	.166	.420
5	0.460	0.600	0.493	.107	0.033	.178	.196	.616
6	0.350	0.493	0.392	.101	0.040	.205	.229	.845
7	0.265	0.392	0.296	.096	0.031	.245	.281	1.126
8	0.195	0.296	0.226	.070	0.031	.236	.270	1.396
9	0.140	0.226	0.172	.054	0.032	.239	.273	1.669
10	0.100	0.172	0.130	.042	0.030	.244	.280	1.949
11	0.070	0.130	0.103	.027	0.033	.207	.233	2.182
12	0.047	0.103	0.075	.028	0.028	.272	.317	2.499

**TABLE 3.3: ROLLING SCHEDULE FOR Al-8Mg**

PASS	MILL GAP (in)	$t_i$ (in)	$t_f$ (in)	$\Delta t$ (in)	MILL DEFLECTION	$e_i$	$\epsilon_i$	$\Sigma \epsilon_i$
1	0.900	1.005	0.936	0.069	0.036	0.069	0.071	0.071
2	0.790	0.936	0.821	0.115	0.031	0.123	0.131	0.202
3	0.680	0.821	0.715	0.106	0.035	0.129	0.138	0.340
4	0.570	0.715	0.602	0.113	0.032	0.158	0.172	0.512
5	0.460	0.602	0.501	0.101	0.041	0.168	0.184	0.696
6	0.350	0.501	0.389	0.112	0.039	0.224	0.253	0.949
7	0.265	0.389	0.299	0.090	0.034	0.231	0.263	1.212
8	0.195	0.299	0.232	0.067	0.037	0.224	0.254	1.466
9	0.140	0.232	0.172	0.060	0.034	0.259	0.288	1.754
10	0.100	0.172	0.134	0.068	0.034	0.395	0.250	2.003
11	0.070	0.134	0.104	0.030	0.034	0.224	0.253	2.257
12	0.047	0.104	0.078	0.026	0.021	0.250	0.288	2.544

### C. TENSILE TESTING

A portion of the rolled material was machined to provide samples for tensile testing. Dimensions are shown in Figure 3.2. An Instron Model TT-D Universal Testing Machine was utilized for tensile testing. The test temperature was maintained by a Marshall Model 2232 clamshell furnace. Samples were placed in preheated grips and the assembly was quickly placed within the clamshell to reach equilibrium at the test temperature (300°C) within 30-40 minutes. Tensile testing was conducted using constant crosshead speeds which provided nominal strain rates between  $6.67 \times 10^{-2}$  and  $6.67 \times 10^{-5} \text{ sec}^{-1}$ .

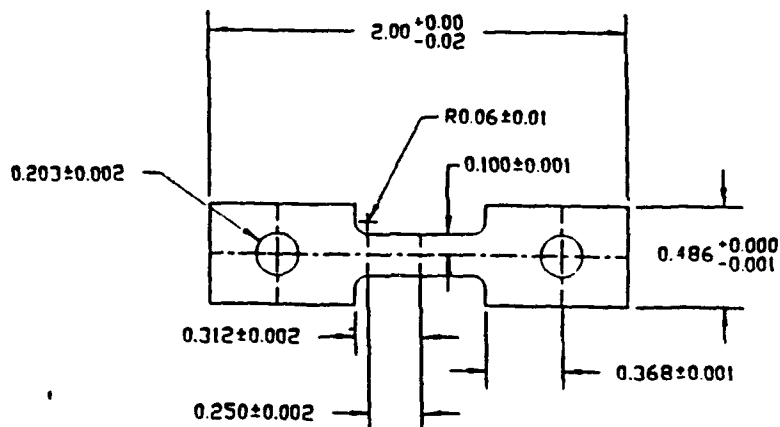


**Figure 3.2 Tensile Test Specimen Design**  
(tolerances are in inches)



#### D. DATA REDUCTION

True stress vs. strain curves were calculated from the Instron chart data which recorded load vs. time. The data were compensated for the variation in strain rate due to use of a constant crosshead speed such that stress vs. strain data are comparable. The correction is outline by Lee and McNelley [Ref.16].

True stress (at a strain  $\epsilon=0.1$ ) vs. strain rate data were plotted on double logarithmic coordinates for each alloy to facilitate determination of the strain rate sensitivity coefficient  $m$ . Also, ductility vs. strain rate data were plotted for comparisons between alloys. Finally, the strain rate sensitivity coefficients and ductility vs. strain rate plots for the Al-10Mg-.1Zr alloy were compared to those of previous work [Ref.8].

#### E. SCANNING ELECTRON MICROSCOPY

Specimens sectioned following the various rolling passes were electropolished for observation in the SEM. The  $\beta$ -phase particle sizes and distributions were characterized with secondary electron images. Backscattered electron imaging methods were used to obtain orientation contrast on the as-polished samples. The orientation of the sample during microscopy, was the transverse longitudinal plane relative to the rolling direction.

#### IV. RESULTS AND DISCUSSION

The first section of this chapter is concerned with a comparison of the mechanical properties achieved for the Al-10Mg-0.1Zr alloy in this work, to the mechanical property data recorded in the previous work of Gorsuch [Ref.10]. Subsequently, the mechanical properties of the Al-8Mg-0.1Zr and Al-8Mg alloys are presented and compared to those of the similarly processed Al-10Mg-0.1Zr alloy from this work. This is followed by a study of the microstructural development during processing of the Al-8Mg-0.1Zr alloy. Finally, the microstructural results of the similarly processed Al-8Mg-0.1Zr and Al-10Mg-0.1Zr alloys are compared at two stages of processing.

It will be seen that the mechanical properties in this research vary slightly from those reported by Gorsuch [Ref.10]. A total rolling strain of 2.5 was used in this as well as in previous studies. However, slight modifications to the rolling schedule were necessary in order to enable sampling after the various intermediate stages of the processing. These alterations are believed to have contributed to differences in the final mechanical properties. Additionally, experimental difficulties encountered with the furnace system used in this work during mechanical testing may also have been a factor.

## A. MECHANICAL PROPERTIES

In Figure 4.1, the results obtained from the tensile testing of the Al-10Mg-0.1Zr alloy are compared to results reported previously by Gorsuch [Ref.10] for this same material. The data is presented as the flow stress at true strain  $\epsilon=0.1$  vs. the strain rate  $\dot{\epsilon}$  on double logarithmic coordinates. It can be seen that both alloys exhibit the same value of  $m \approx 0.36-0.37$ . However, the material processed by Gorsuch [Ref.8] studies is slightly weaker than that processed in this research. This difference in strength persists throughout the range of strain rates investigated. In Gorsuch's [Ref.10] work, it was noted that the material was weakest at small strains, (i.e., at  $\epsilon=0.02$ ), and also exhibited a higher  $m$  value at smaller strain values. Additionally, Gorsuch [Ref.10] noted that  $m$  decreased with increasing strain. These observations were attributed to grain coarsening size during superplastic straining. A greater increase in grain size (per unit strain) at lower strain rates may account for the decrease in  $m$ -value with strain.

The flow stress in superplastic materials is generally recognized to depend inversely on the grain size to a power 2 or 3, as discussed earlier in Chapter II of this work. It is likely that the grain size in the material processed in this research is coarser than that achieved by Gorsuch [Ref.10].

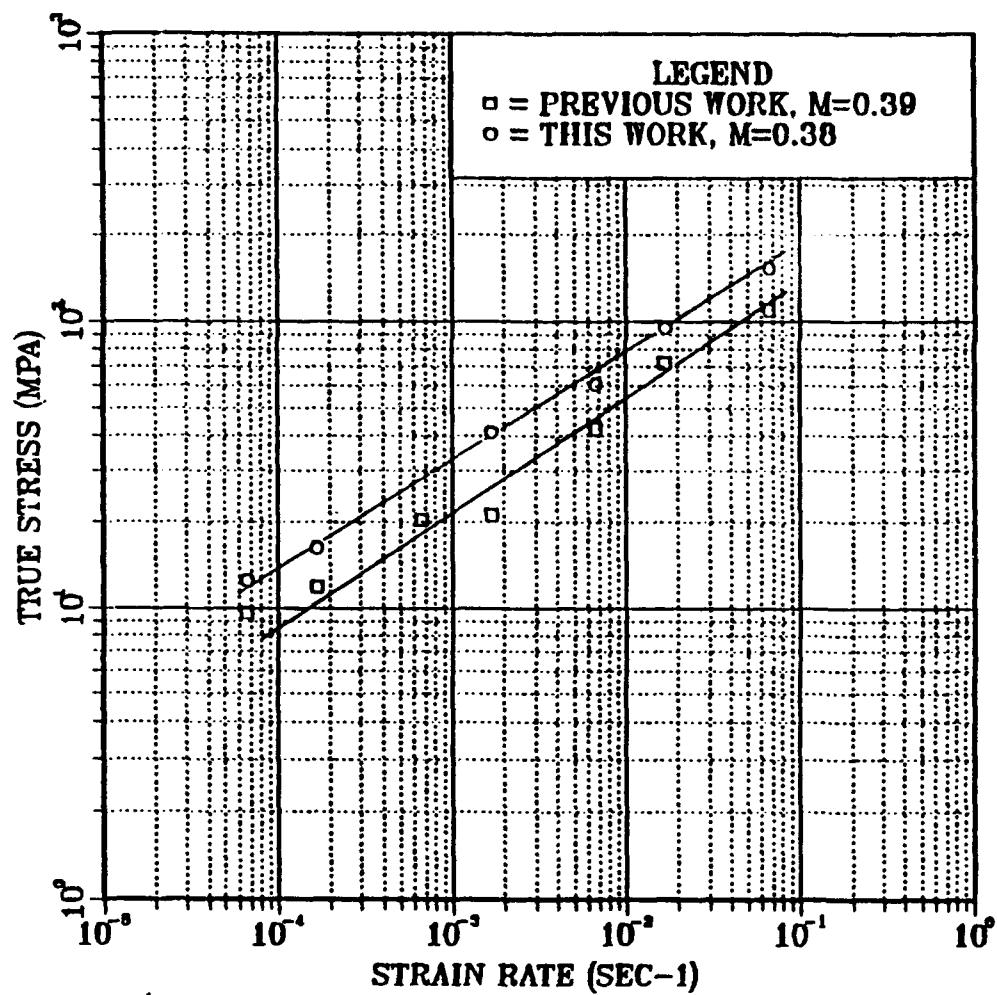


Figure 4.1 Strain rate coefficient for Al-10Mg-0.1Zr compared with previous work.

The mechanical properties of the three alloys of this study are compared in Figure 4.2. The data is again compared as flow stress at a strain  $\epsilon=0.1$  vs. strain rate  $\dot{\epsilon}$ , on double logarithmic coordinates. Note that the higher Mg-alloy, is the weakest, softest material of the three. It is also the most rate sensitive at this value of strain. The Al-8Mg-0.1Zr alloy is stronger and less strain rate sensitive compared to the Al-10Mg-0.1Zr alloy. The Al-8Mg alloy is the strongest of the three at all strain rates but has a similar strain rate sensitivity coefficient when compared to the Al-8Mg-0.1Zr alloy.

These data suggest that the Al-10Mg-0.1Zr alloy is the finest microstructure of the three (recall that grain refinement weakens a superplastic material). This is consistent, in turn, with a higher  $\beta$ -phase content and therefore a smaller  $\beta$ -phase particle spacing which would lead to a finer recrystallized grain size during processing. The corresponding ductility vs. strain rate data for these three alloys are shown in Figure 4.3. The ductility vs. strain rate response reflects the strength data, in that the most ductile material is the Al-10Mg-0.1Zr alloy. In the current research the peak ductility observed was 700%, while Gorsuch [Ref.8] reported a peak ductility of about 1100% (Figure 4.4). The lower ductility in this research likely reflect the slight change in processing procedures which were necessary in order

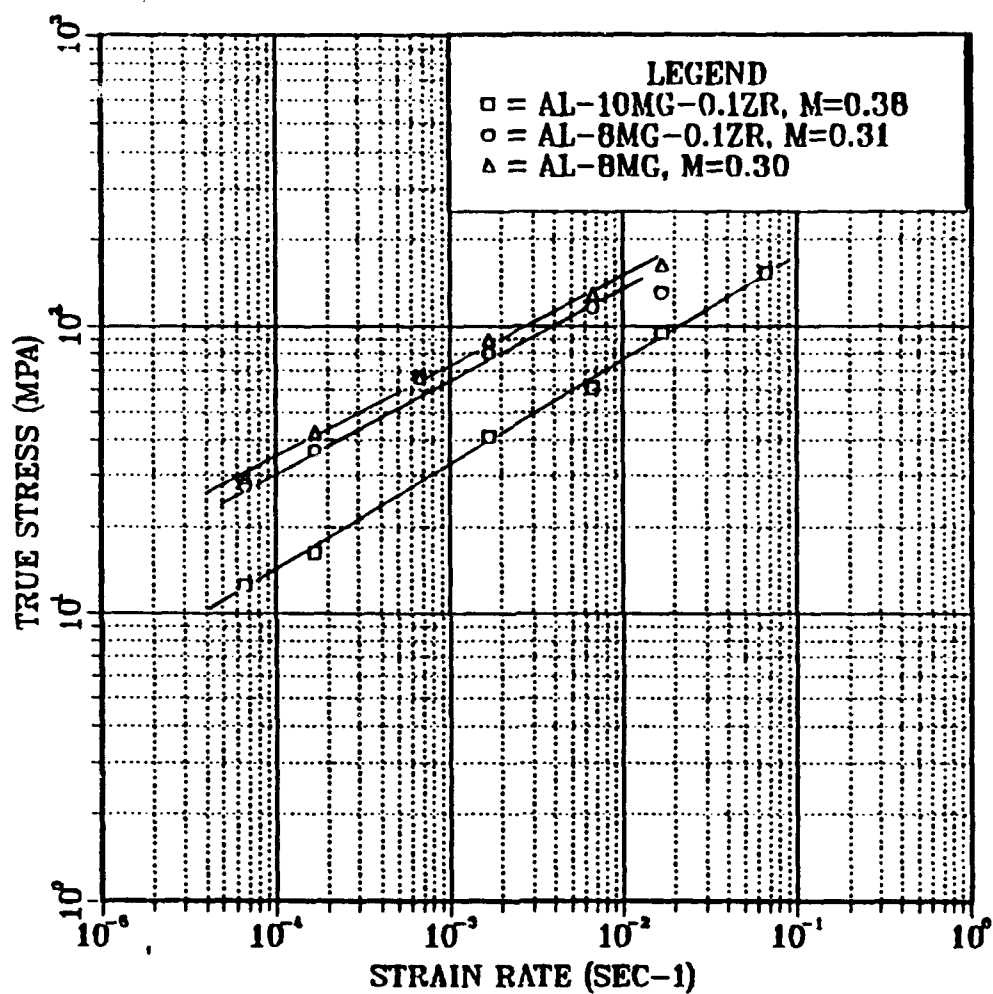


Figure 4.2 Strain rate sensitivity coefficient  $m$  for  
TMPs Al-10Mg-0.1Zr, Al-8Mg-0.1Zr and Al-8Mg

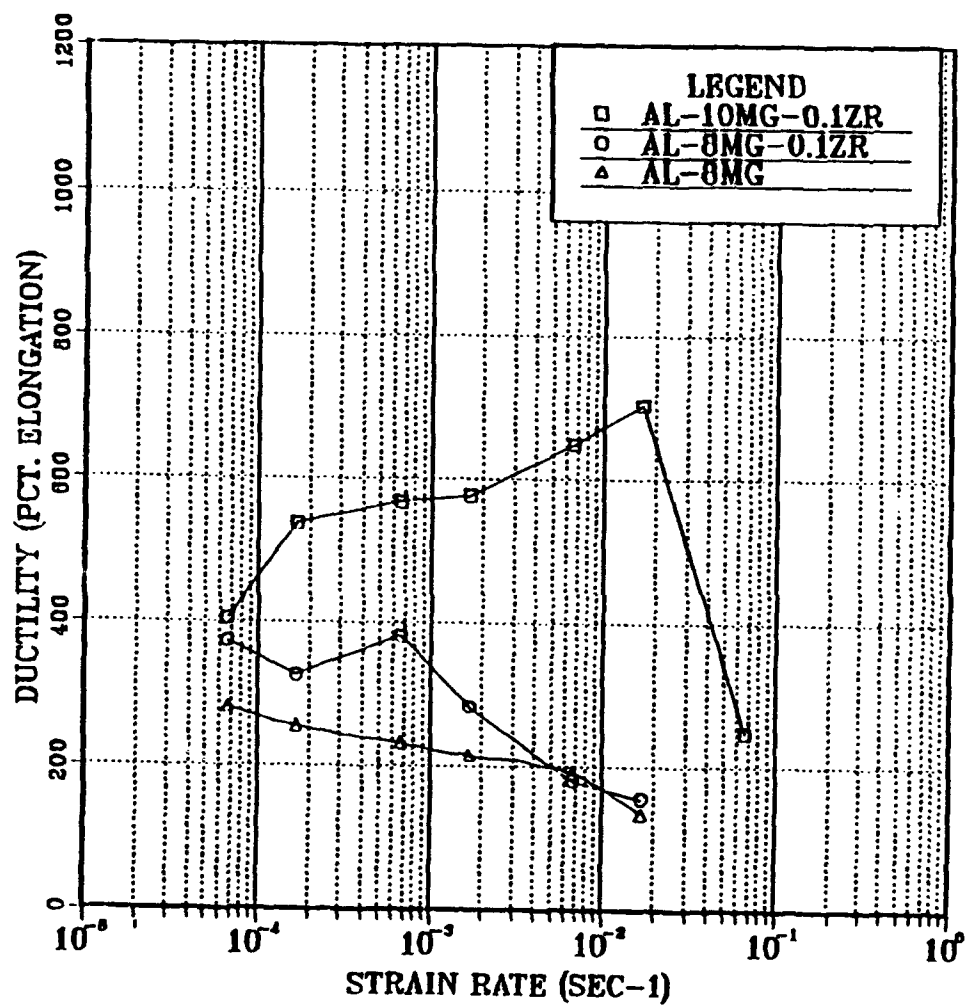


Figure 4.3 Ductility vs strain rate for TMPs  
Al-10Mg-0.1Zr, Al-8Mg-0.1Zr & Al-8Mg

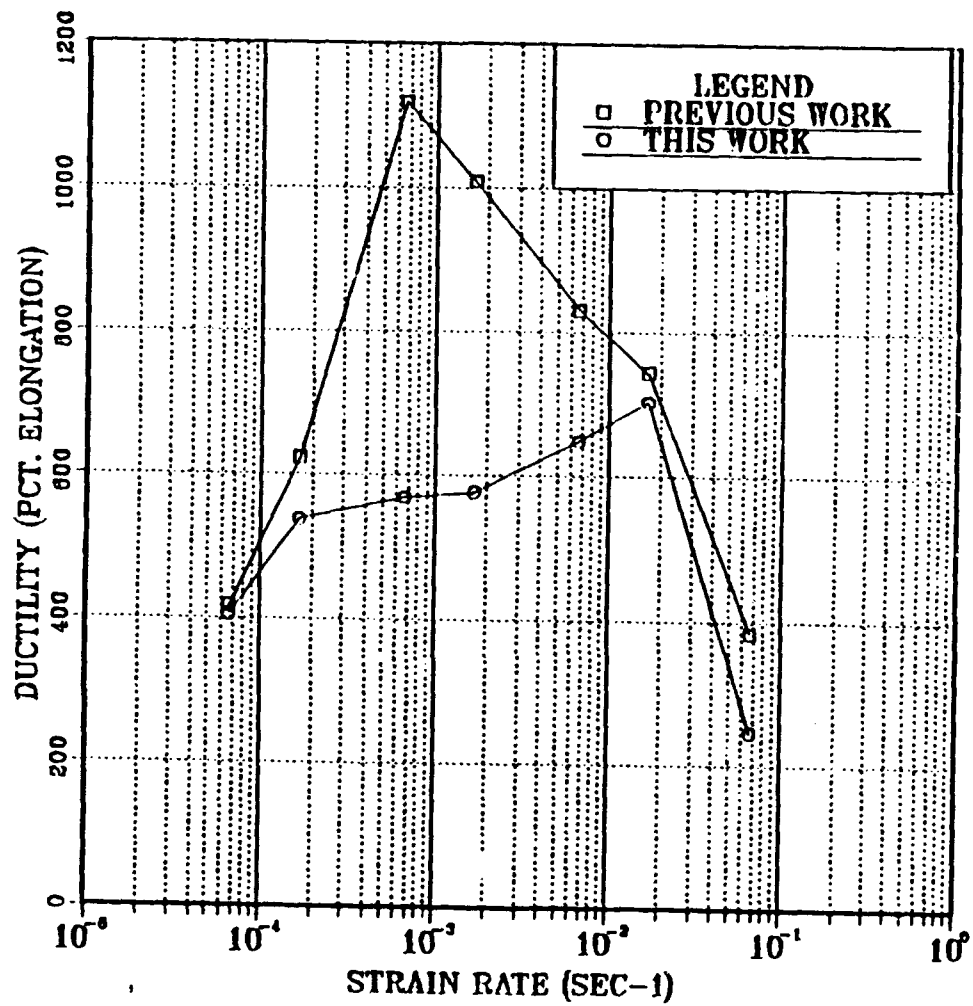


Figure 4.4 Ductility vs strain rate for TMP Al-10Mg-0.1Zr  
(compared to previous work)



to acquire samples at various stages (as discussed earlier in this chapter). The ductility data for the 8.0Mg materials exhibited considerably lower elongations. Superplastic elongations were obtained for the binary alloy only at the slowest strain rates and are just barely in the superplastic regime. The 8Mg-0.1Zr alloy does appear to provide superplastic elongations, at least for strain rates up to about  $10^{-3} \text{ s}^{-1}$ , with peak elongations of about 375%. This is attributable to the Zr addition. In general, the lower ductility of the 8Mg-alloys likely reflects a coarser grain structure achieved in processing in turn due to a lower  $\beta$ -phase content.

These data compare reasonably well with previous studies. As discussed earlier, discrepancies in strengths and ductilities may be related to the steps used to obtain samples representing the various intermediate stages of the processing. On the other hand, the strain rate sensitivity coefficient value and the ductility dependence on composition are all consistent with previous work.

**B. ANALYSIS OF MICROSTRUCTURAL EVOLUTION DURING PROCESSING OF  
Al-8Mg-0.1Zr**

As described in the experimental procedure section, samples were obtained representing the as-rolled condition of the material after each of several passes as summarized in Table 4.1. The accumulated rolling strain is also included in this table. In addition, a portion of each of these samples was given an annealing treatment of 25 minutes duration in order to allow the examination of the effect of IPA. That is, the material processed for pass 6 and then annealed for 25 minutes will then represent the structure present just prior to pass 7. The analysis of microstructure was conducted using BSI in the SEM with samples prepared to facilitate observation of both orientation contrast and the  $\beta$  particles. The presentation of this data will be in the order of the passes in Table 4.1.

**TABLE 4.1: ROLLING PASSES WHERE SAMPLES WERE ACQUIRED**

MATERIAL	3RD	6TH	8TH	10TH	12TH
Al-10Mg-0.1Zr	0.403	1.023	1.515	2.043	2.601
Al-8Mg-0.1Zr	0.254	0.845	1.396	1.949	2.500
Al-8Mg	0.340	0.949	1.466	2.003	2.544

1. As-rolled condition, pass 3 ( $\epsilon=0.254$ ):

Figure 4.5.a shows a BSI micrograph obtained for as-rolled material following 3 passes. The  $\beta$ -phase appears to have precipitated only onto the prior grain boundaries present in the original solid solution. The particles form a nearly continuous phase along the boundaries as shown in Figure 4.5.b, a portion of such a boundary shown at a higher magnification. Note here that the particle sizes is on the order of 1-2  $\mu\text{m}$ .

The features imaged within the grains are microbands which are oriented differently in the adjacent grains as seen in Figure 4.5.b. This orientation change reflects the misorientation of the lattice across the grain boundary. The observed pattern of intersecting bands in the upper grain may be due to the operation of different slip systems in successive passes as the lattice rotates during straining.



**Figure 4.5** a) Backscattered electron micrograph showing Al-10Mg-0.1Zr following pass 3 in the as-rolled condition; b) depicts a region in 4.5.a at a higher magnification.

## 2. Annealed condition, after pass 3 ( $\epsilon=0.254$ ):

Upon annealing, the  $\beta$ -phase precipitate appears to form along some but not all of the microband boundaries in the structure. Figures 4.6 (a & b) show examples of the onset of precipitation in association with these microband deformation structures. Precipitates are still evident along the prior boundaries as well. Also, the microband structure appears to break up into more nearly equiaxed subgrains during annealing. An additional feature of the developing microstructure was noted and is seen in figure 4.6.c, which shows at a higher magnification a region nearby the grain boundary in figure 4.6.b. Nearby where microbands terminate at a grain boundary, there appears to be evidence of substructure formation. The precipitation of the  $\beta$ -phase on the microband boundary within the grain interior is clearly seen. Also, this micrograph suggests the development of a precipitate-free zone in the vicinity of the prior boundary. This would result from the formation of the  $\beta$ -phase on prior grain boundaries with the absorption of Mg from an envelope on either side of the grain boundary. Then, subsequent precipitation on the microbands within the grain interior can not occur for a distance into the grain. Additionally, there appear to be well defined, equiaxed features which may be recovered structures or nuclei of new grains forming in the vicinity of the grain boundary precipitate particles.

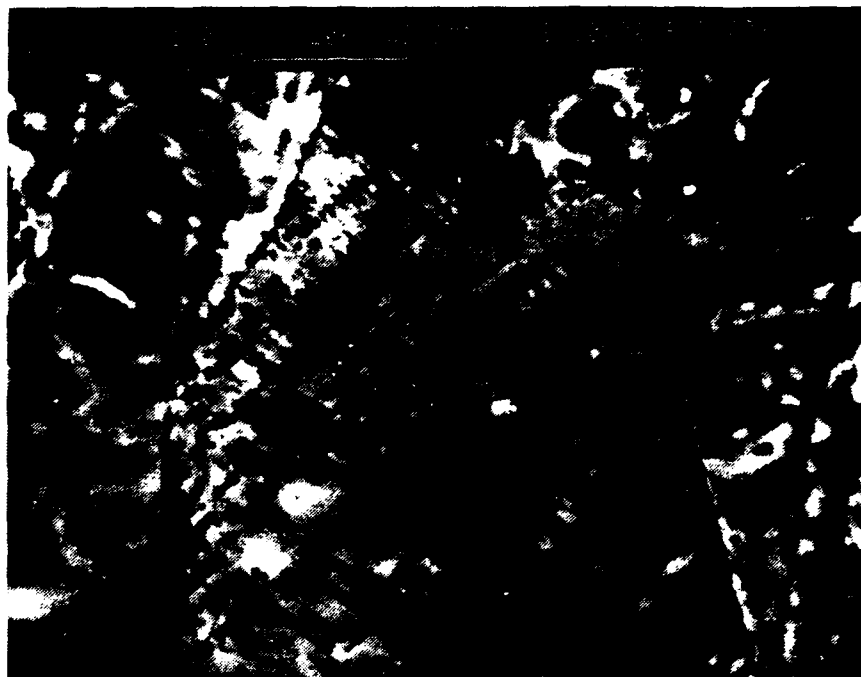
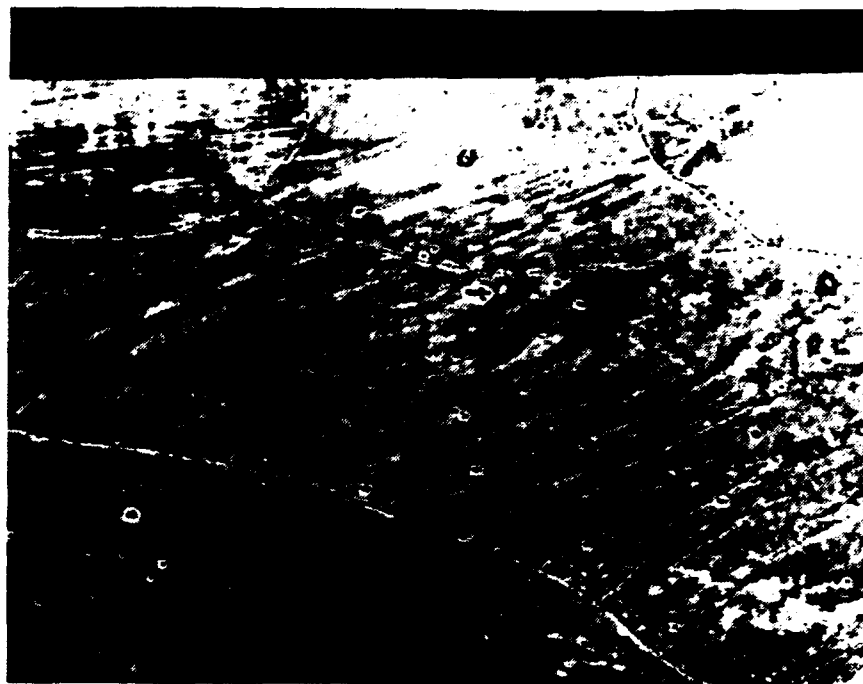


Figure 4.6 a & b Backscattered electron micrographs showing Al-8Mg-0.1Zr following pass 3; after 25 minutes annealing at 300°C.



**Figure 4.6.c** Backscattered electron micrograph showing Al-8Mg-0.1Zr following pass 3; a section of 4.5.b at higher magnification

### 3. As-rolled condition, Pass 6 ( $\epsilon=0.845$ ):

As can be seen in Figure 4.7, the most significant microstructural change compared to the earlier stage of the processing is the flattening of the original grains in a "pancake" like manner. The presence of the  $\beta$ -phase particles on prior boundaries is still evident and these particles appear to be extending and separating in the direction of rolling as the grain shape changes. Within the grain interiors the microbands observed earlier are still evident and in many cases there appear to be secondary sets of these bands forming at an angle to the first. That is, within the first set (or "first-order") of microbands (formed in earlier stages) there appears to be a more refined second set (or "second order") of microbands, the extent of which appears to be confined within the first order microbands. It is also apparent that the boundaries of some of these bands serve as precipitation sites whereas others have yet to support the formation of any of the  $\beta$ -phase.



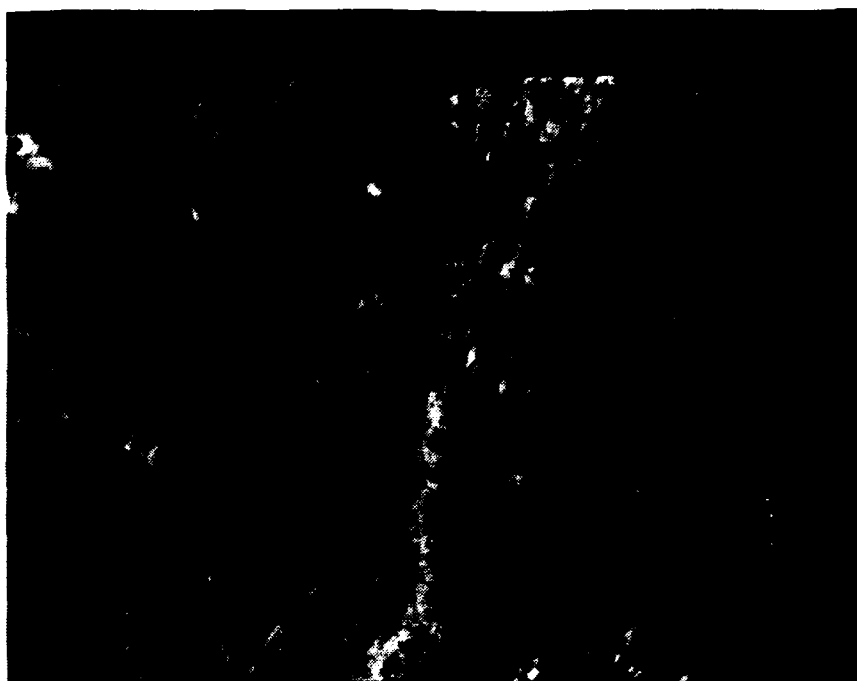


**Figure 4.7** Backscattered electron micrograph of Al-8Mg-0.1Zr following pass 6; in the as-rolled condition.

#### 4. Annealed condition, after pass 6 ( $\epsilon=0.845$ ):

In Figure 4.8.a, significant changes in structure are now seen. Increasingly well developed substructures are now apparent, as reflected in the more sharply defined orientation contrast from region to region within prior microbands. That is, dislocations are apparently forming well defined subgrain boundaries, and increased orientation contrast suggests that the boundaries are of higher misorientations than in earlier stages in the process. Precipitation is also occurring more extensively on boundaries of prior microbands throughout the structure. The formation of increasingly well defined substructures is apparent in Figure 4.8 (b & c) as well as an increase in precipitation within this structure. There is evidence that some larger particles located at prior boundaries are becoming sites for PSN of recrystallization. These particles are approaching 1  $\mu\text{m}$  in size, a size recognized as the minimum necessary for PSN [Ref.21] However the structure remains predominately recovered and not recrystallized.

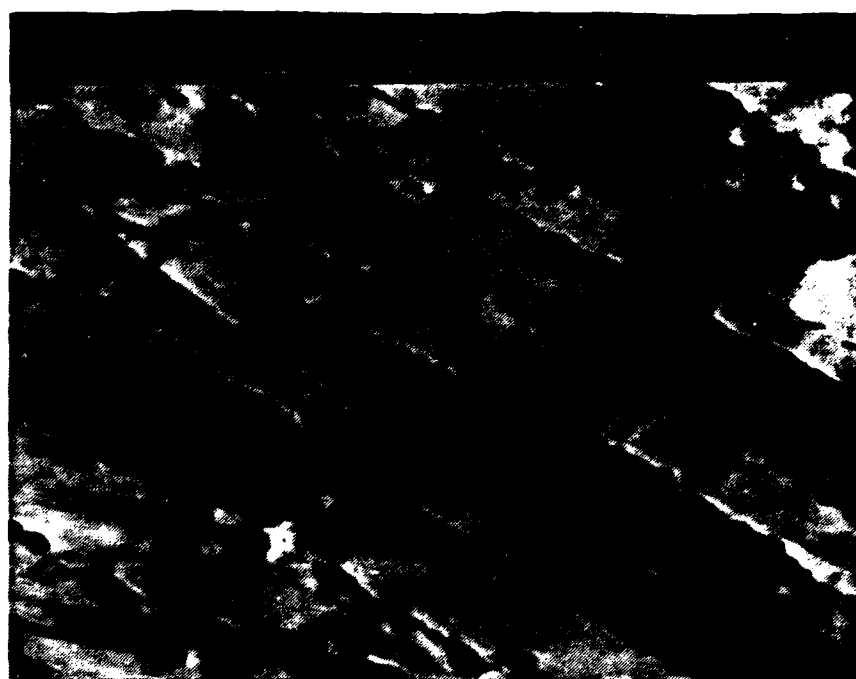


**Figure 4.8** a) Backscattered electron micrograph of Al-8Mg-0.1Zr following pass 6; after 25 minutes of annealing b) a section of 4.8.a at a higher magnification

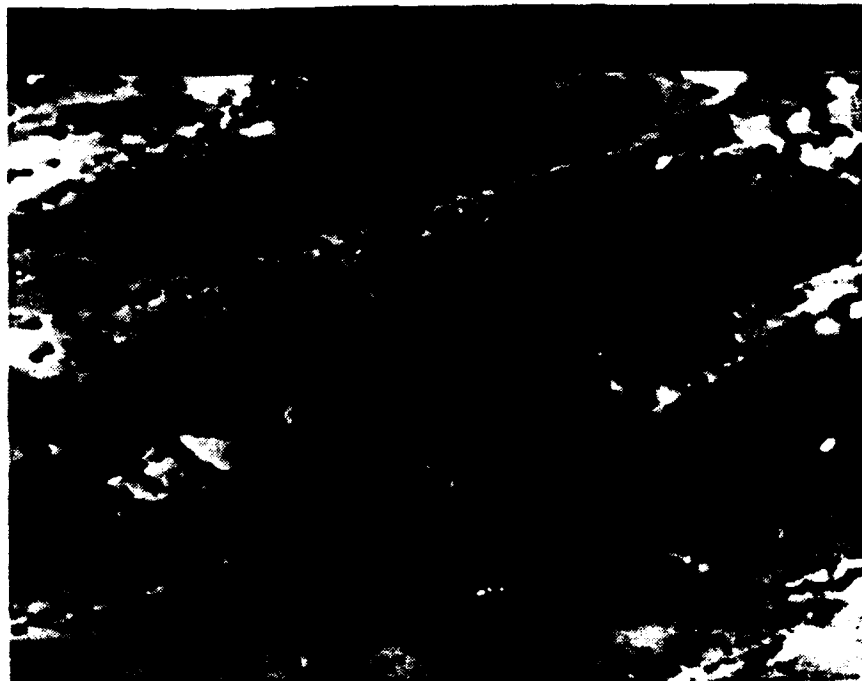


**Figure 4.8.c** Backscattered electron micrograph of Al-8Mg-0.1Zr following pass 6; depicts a section of 4.8.a at higher magnification.

5. As-rolled condition, pass 8 ( $\epsilon=1.396$ ):

Similar microstructural features are apparent after 8 rolling passes as were noted after 6 rolling passes. Precipitation is still apparent in association with the first order bands. These bands are apparently rotating and becoming more nearly parallel to the rolling direction. Higher order bands continue to be observed within lower order bands. Precipitation is also beginning on the higher order bands.



Figure 4.9.a Backscattered electron micrograph showing Al-8Mg-0.1Zr following pass 8; in the as rolled condition.

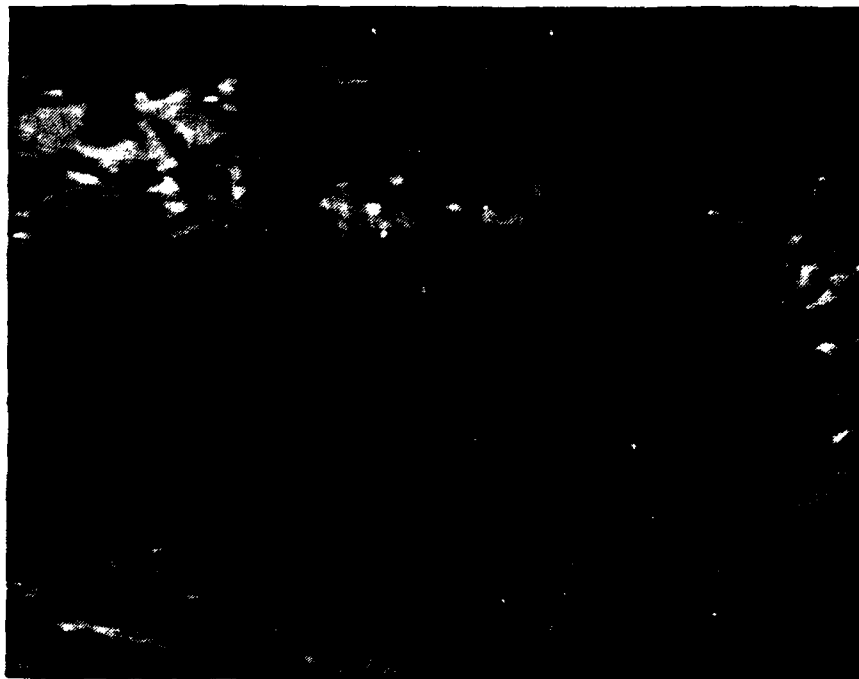


Figure 4.9 b) BSE-scattered electron micrograph of Al-8Mg-0.1Zr following pass 8; in the as-rolled condition; c) depicts region of 4.9.b at higher magnification

#### 6. Annealed condition after pass 8 ( $\epsilon=1.396$ ):

Upon annealing after pass 8, the microstructure in many regions is evolving into an increasingly well defined and equiaxed condition. Figure 4.10.a. shows a region in which such a well defined equiaxed structure is apparent. In such regions the precipitate particles are more uniformly distributed and the band-like nature of the initial precipitation is no longer as readily apparent. The particles are approaching 1  $\mu\text{m}$  diameter and are corresponding more closely spaced. The microbands of earlier stages are no longer apparent, suggesting that the particles are altering the deformation mode. The increasing orientation contrast suggests still more highly misoriented subgrains at this stage compared to earlier stages. However, the microstructure is still not uniform and there are regions in which little or no precipitation has occurred (Figure 5.6.b). This non-uniformity, which is apparent in comparing Figures 4.10.a and 4.10.b, demonstrates the value of the backscattering imaging modes with bulk samples. In preparation of thin foils for TEM, it is entirely possible that one or the other but not both of these regions would be observed, given the selective nature of penetration during thin foil preparation.

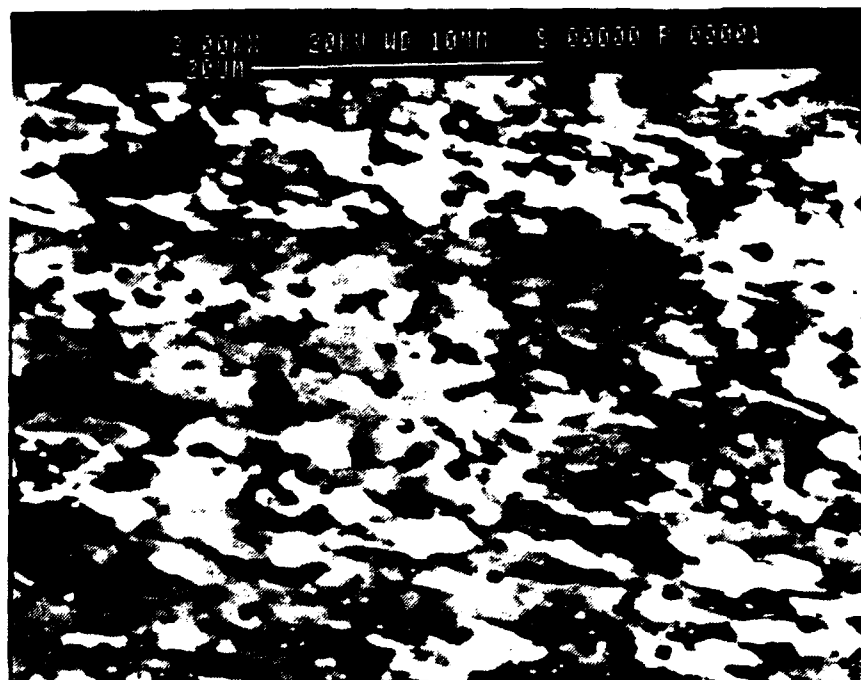


Figure 4.10 a) Backscattered electron micrograph showing Al-8Mg-0.1Zr following pass 8; after 25 minutes of annealing at 300°C. b) at higher magnification.





**Figure 4.10.c** Backscattered electron micrograph of Al-8Mg-0.1Zr following pass 8; after 25 minutes of annealing; region of very little precipitation.

**7. As-rolled condition, pass 10 ( $\epsilon=1.949$ ):**

The same patterns are observed after 10 rolling passes. The volume fraction of particles does not appear to have increased beyond that observed after 8 passes. It is notable that there appears to be a more nearly continuous contrast variation in the vicinity of some particles. This may reflect the development of local lattice rotations around particles (Figure 4.11).



**Figure 4.11 Backscattered electron micrograph of Al-8Mg-0.1Zr following pass 10; in the as-rolled condition.**

**8. Annealed condition after pass 10 ( $\epsilon = 1.949$ ):**

The microstructure remains rather nonuniform even after processing as far as 10 rolling passes. The particles are still not uniformly distributed throughout the microstructure (Figure 4.12). In regions of higher particle concentrations, the microstructure appears to be more nearly equiaxed and uniform after annealing. The banded nature of the microstructure is more apparent in regions where fewer particles have precipitated.

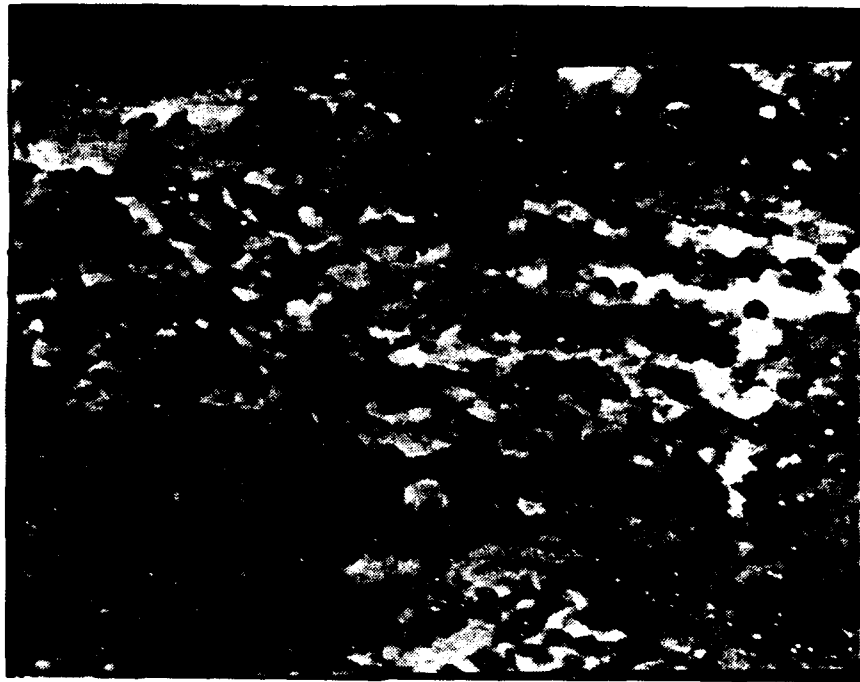


**Figure 4.12 Backscattered electron micrograph showing Al-8Mg-0.1Zr following pass 10; after 25 minutes of annealing at 300°C.**

9. As-rolled condition, pass 12 ( $\epsilon=2.5$ ):

After the final rolling pass a well-defined substructure is now readily apparent even in the as rolled condition (Figure 4.13). There is also continuous contrast variation in the immediate vicinity of the particles, suggesting the formation of deformation zones and local lattice rotation around them. The substructure represents that retained from previous passes and this suggests that there is a cumulative effect of the processing and a build up of such structures during the sequence of deformation and annealing cycles.



Figure 4.13 Backscattered electron micrograph of Al-8Mg-0.1Zr following pass 12; in the as-rolled condition.

10. Annealed condition after pass 12 ( $\epsilon=2.5$ ):

Upon annealing after the final rolling pass, the elongated or band like nature of the microstructure is still apparent. In this particular sample, there appears to be little evidence of PSN in association with some of the largest particles, (for instance, at the bottom center of the micrograph Figure 4.14). In some regions relatively fine grains are now appearing, although in general the microstructure still retains the appearance of recovered substructure rather than an equiaxed grain structure.

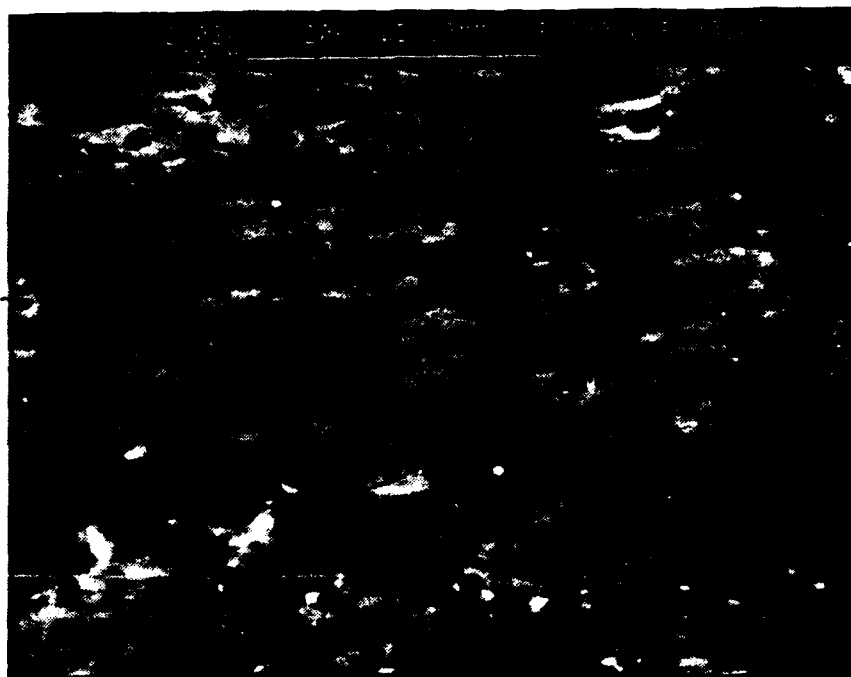


Figure 4.14 Backscattered electron micrograph showing Al-8Mg-0.1Zr following pass 12; after 25 minutes of annealing at 300°C.

### C. COMPARISONS OF Al-10Mg-0.1Zr AND Al-8Mg-0.1Zr AFTER THE 3rd AND 12th PASSES

In the final part of this research, microstructural comparisons were made between the higher Mg content alloy (Al-10Mg-0.1Zr) and the lower Mg content alloy (Al-8Mg-0.1Zr), concentrating on the 3RD and 12TH rolling passes. In research by Rogers [Ref.11], a more detail analysis of the Al-10Mg-0.1Mg alloy was completed.

#### 1. As rolled condition, pass 3 ( $\epsilon=0.403$ ):

Figure 4.15. (a & b), presents micrographs of the Al-10Mg-0.1Zr alloy after the 3rd rolling pass. In comparing these data to those of Figures 4.5. (a & b), it is readily apparent that the volume fraction of  $\beta$  phase is greater in the higher Mg content alloy. This is expected since the processing temperature of 300°C is below the solvus for both alloys and the higher Mg content should result in the greater driving force for precipitation and a higher volume fraction of  $\beta$ -phase at equilibrium. AS in the lower Mg alloy, precipitation is clearly evident along prior grain boundaries. However, in the higher Mg alloy additional precipitation within the grain interior is clearly evident and appears to occur in association with microbands. Some precipitation not associated with microbands may have occurred as well.

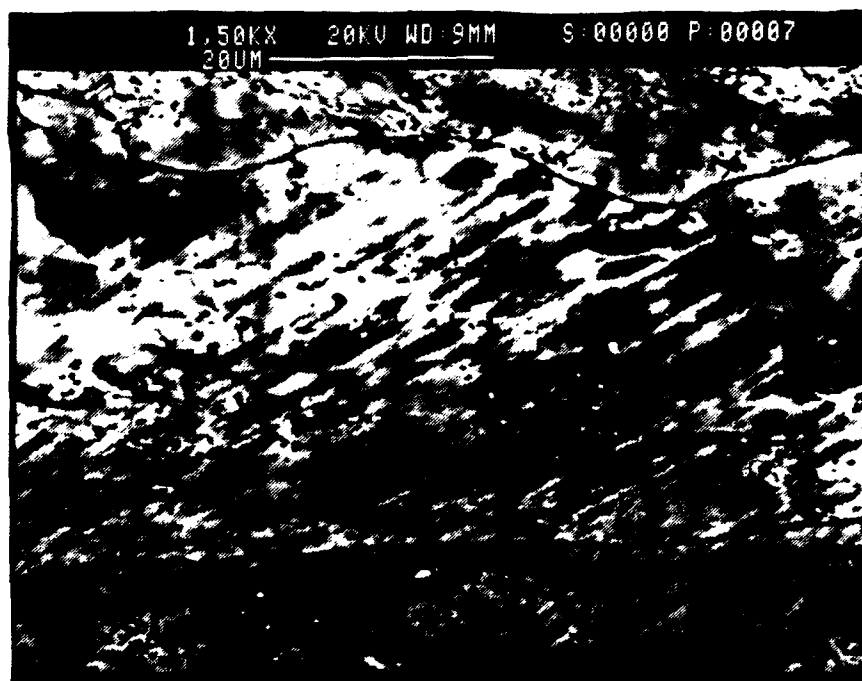
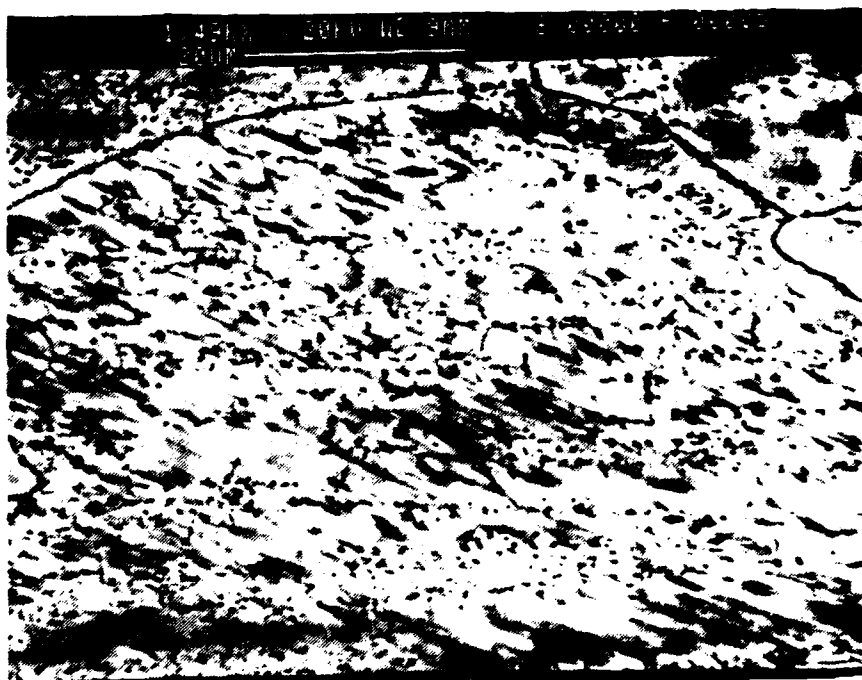


Figure 4.15.a Backscattered electron micrographs showing Al-10Mg-0.1Zr following pass 3; in the as-rolled condition.



Figure 4.15.b Backscattered electron micrograph of Al-10Mg-0.1Zr following pass 3; in the as-rolled condition



## 2. Annealed condition after pass 3 ( $\epsilon=0.403$ ):

Upon annealing after the 3rd pass the volume fraction of  $\beta$  phase increases greatly when compared to the condition prior to annealing. Comparing Figure 4.16 with 4.6 (a & b), the  $\beta$  phase is much more uniformly distributed throughout the grain interiors, appearing to occur both in association with the band like features and also as equiaxed particles not associated with such bands. In Figure 4.6 (a & b), all the  $\beta$  particles seemed to be associated with microbands. Finally, in some instances, the  $\beta$  particles in the higher Mg alloy are elongated in nature. The reason for such shapes is not clear.

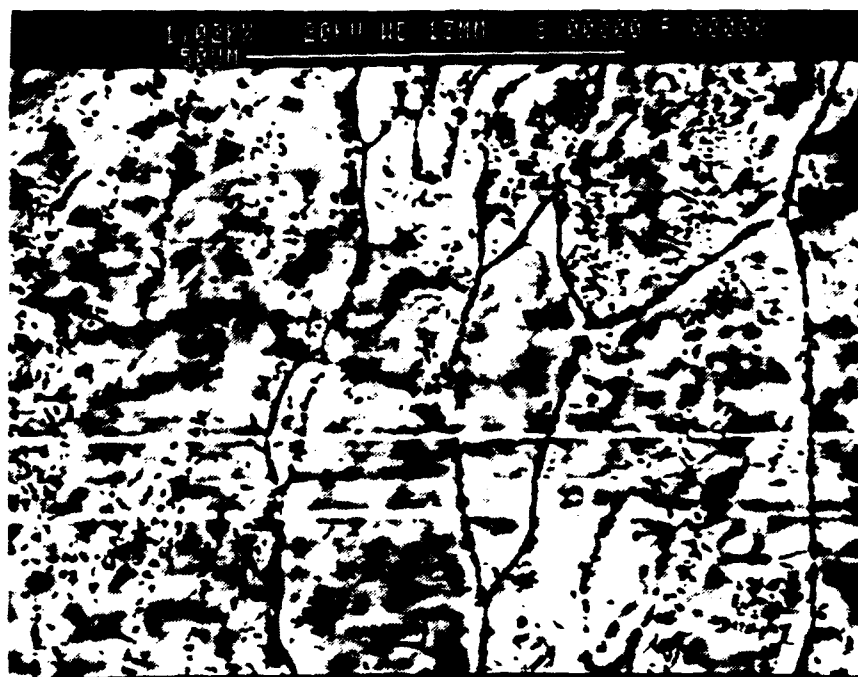
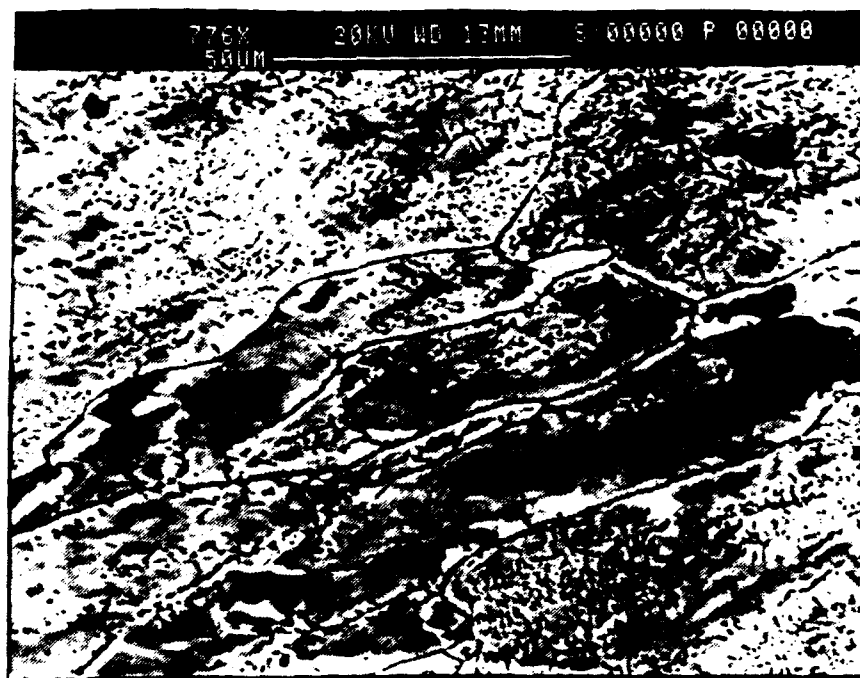
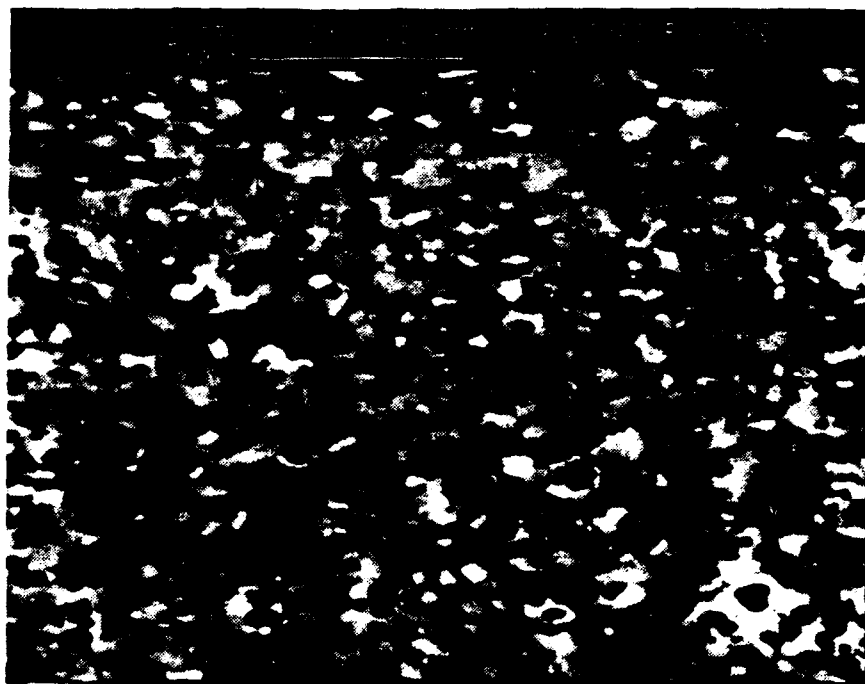


Figure 4.16 Backscattered electron micrographs showing Al-10Mg-0.1Zr following pass 3; after 25 minutes of annealing at 300°C.

3. As-rolled condition, pass 12 ( $\epsilon=2.6$ ):

Again, the precipitation is much more general in the higher Mg-alloy. Notice also in Figure 4.17, that the higher Mg alloy exhibits a fine grain structure with very little, if any, evidence of the band structure that persisted throughout and was present at the conclusion of the processing, for the lower Mg content alloy (Figure 4.9). It is also clear that the  $\beta$  phase volume fraction is higher in 4.17, and that there is a homogenous distribution of larger particles.



**Figure 4.17** Backscattered electron micrographs of  
Al-10Mg-0.1Zr following pass 12; in the as-rolled  
condition

#### 4. Annealed condition, after pass 12 ( $\epsilon=2.6$ ):

In comparing micrographs of the two alloys after 25 minutes of annealing following the final rolling passes, it can readily be seen why the 10Mg-alloy exhibited a much higher ductility than the 8Mg-alloy during mechanical testing. The micrograph of the Al-10Mg-0.1Zr alloy in Figure 4.18, clearly reveals a homogenous particle distribution with well-defined contrast and a fine, equiaxed microstructure. The micrograph of Al-8Mg-0.1Zr alloy (Figure 4.14), showed a recovered and elongated substructure rather than an equiaxed grain structure, with only a few regions exhibiting relatively fine grains.

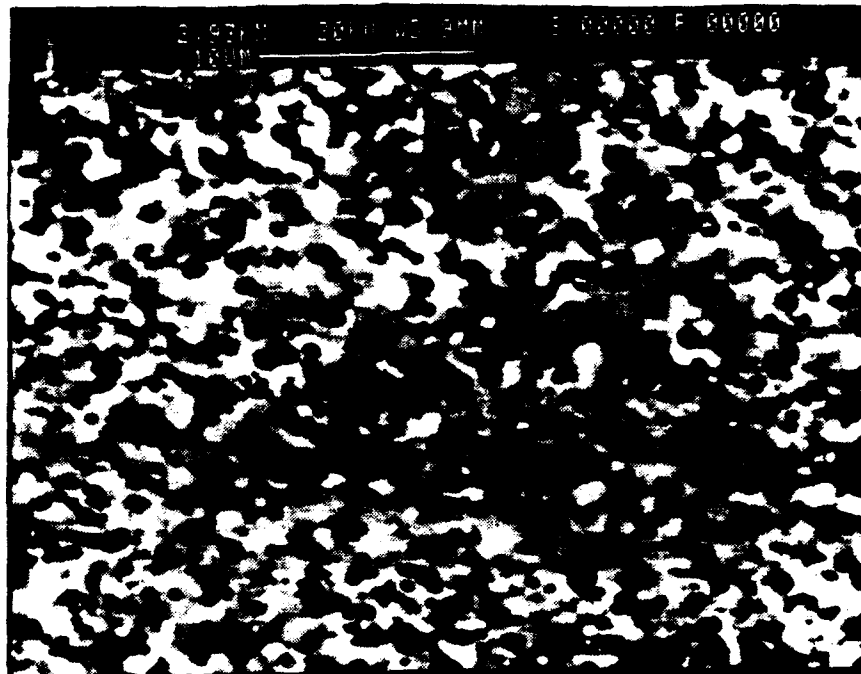


**Figure 4.18** Backscattered electron micrograph of Al-10Mg-0.1Zr following pass 12; after 25 minutes of annealing at 300°C.

## V. CONCLUSIONS AND RECOMMENDATIONS

### A. THE FOLLOWING ARE THE MAIN CONCLUSIONS OF THIS WORK.

1. Thermomechanical processing of the Al-8Mg, Al-8Mg-0.1Zr and Al-10Mg-0.1Zr alloys at 300°C, to a strain of 2.5 and with 30 min annealing time in between passes, resulted in maximum ductilities of 250%, 475%, and 700%, respectively. Though the processing was the same for all three, the extent of superplasticity varied, suggesting that different materials may require different combinations of processing parameters for superplasticity.

2. The lower ductility attained here for the Al-10Mg-0.1Zr alloy in spite the use of the same parameters as Gorsuch [Ref.10] may have been caused by: (a) slight modifications to the rolling schedule, (b) the brief interruption of the rolling process (1 min) to take samples, and (c) the non-optimal temperature control during testing.

3. Microstructural evolution in Al-8Mg-0.1Zr can be described by the sequence: (a) precipitates form on the boundary of the initial solid solution; (b) subsequent rolling produces microbands, (c) precipitates form, but only on some bands; (d) in between the bands there is substructure; (e) secondary bands form and precipitates form on them; (f) the structure begins to loose its band-like nature and become

equiaxed in appearance as the particles precipitate on bands and PSN tends to break up the band structure; (g) in subsequent rolling passes a homogenizing of the structure take place; (h) grain elongation remain apparent throughout processing; (i) bands become more refined in later stages; (j) PSN is limited in extent and recovery appears predominant in the final structure.

4. In comparing the microstructure of the Al-8Mg-0.1Zr and the Al-10Mg-0.1Zr alloys, the 10Mg alloy exhibited much more extensive precipitation after earlier in the rolling. After the conclusion of rolling, it has a much finer grain structure, and the volume of  $\beta$  is higher and improved superplastic response results.

**B. The following are recommended for future work**

1. Further investigations of the evolving microstructure in the Al-10Mg-0.1Zr alloy.

2. A complete and quantitative assessment of grain size and particle size throughout the process.

3. The misorientation and character of boundaries produced during process should be evaluated.



### LIST OF REFERENCES

1. Bly, D. C., Sherby, O. D., and Young, C. M., "Influence of Thermal Mechanical Treatments on the Mechanical properties of a Finely Spheroidized Eutectic composition Steel," Material Science and Engineering, Volume 2, pp. 41-46, 1973.
2. Askeland D. R., The Science and Engineering of Materials, 2nd Edition, p.210, 1989.
3. Sherby, O. D., Wadsworth, J., Development and Characterization of Fine Grain Superplastic Materials, pp. 355-387.
4. Ness, F. G., Jr., High Strength to Weight Aluminum-18 Weight Percent Magnesium Alloy Through Thermomechanical Processing, M. S. Thesis, Naval Post Graduate School, Monterey, California, December 1976.
5. Birgay, C. P., Microstructural Response of Aluminum-Magnesium Alloys to Thermomechanical Processing, M. S. Thesis, Naval Post Graduate School, Monterey, California, December 1977.
6. Glover, T. L., Effects of Thermomechanical Processing of Aluminum-Magnesium Alloys Containing High Weight Percent Magnesium, M. S. Thesis, Naval Post Graduate School, Monterey, California, December 1977.
7. Grandon, R. A., High Strength Aluminum-Magnesium Alloys: Thermomechanical Processing, Microstructural and Tensile Mechanical Properties of High Strength Aluminum-Magnesium Alloys, M. S. Thesis, Naval Post Graduate School, Monterey, California, March 1980.
8. Chestermen, C. W., Jr., Precipitation, Recovery, and Recrystallization Under Static and Dynamic Conditions for High Magnesium Aluminum-Magnesium Alloys, M. S. Thesis, Naval Post Graduate School, Monterey, California, March 1980.
9. McNelley, T. and Garg, A., "Development of Structure and Mechanical Properties in Al-10.2%Mg by Thermomechanical Processing," unpublished research, Naval Postgraduate School, Monterey, California.

10. Gorsuch, T. E., The Roles of Strain and Reheating Interval in Continuous Recrystallization During the Thermomechanical Processing by Warm Rolling of Al-Mg Alloy, M. S. Thesis, Naval Post Graduate School, Monterey, California, December 1989.
11. Rogers, S. A., The Role of Particles in Recrystallization of a Thermomechanically Processed Al-Mg Alloy, M. S. Thesis, Naval Post Graduate School, Monterey, California, December 1989
12. Metals Handbook, Desk Edition, American Society for Metals, 1985.
13. Williams, J. C. and Starke, E. A., Jr., The Role of Thermomechanical Processing in Tailoring Properties of Aluminum and Titanium Alloys, p.294.
14. Watts, B. M., Stowell, M. J., Baikie, Owen, D. G. E., Metal Science., 10 (1976), PP. 189-197.
15. Watts, B. M., Stowell, M. J., Baikie, Owen, D. G. E., Metal Science., 10 (1976), PP. 198-205.
16. Mondolfo, L. F., Aluminum Alloys: Structure and Properties, Butterfield and Co. (Publishers) 1976.
17. Lee, E. W. and McNelley, T. R., "Microstructure Evolution During Processing and Superplastic Flow in a High Magnesium Al-Mg Alloy," Materials Science and Engineering, v. 93, 1987
18. Crooks, R., Kalu, P. N., and McNelley T. R., Use of Backscattered Electron Imaging to Characterize Microstructure of a Superplastic Al-10Mg-0.1Zr Alloy, 1991
19. Loretto, M. H., Electron Beam Analysis of Materials
20. Gabriel, B. L., SEM: A User's Manual for Material Science
21. Humphreys, F. J., Aeta Metallurgica, v. 27, p.1801, 1979

## INITIAL DISTRIBUTION LIST

- |  |   |
|--|---|
| 1. Defense Technical Information Center<br>Cameron Station<br>Alexandria, VA 22304-6145  | 2 |
| 2. Library, Code 52<br>Naval Post Graduate School<br>Monterey, CA 93943-5002   | 2 |
| 3. Department Chairmen, Code PH/WH<br>Department of Physics<br>Naval Post Graduate School<br>Monterey, CA 93943-5000                 | 1 |
| 4. Professor T. R. McNelley, Code ME/Mc<br>Department of Mechanical Engineering<br>Naval Post Graduate School                        | 6 |
| 5. Dr. P. N. Kalu<br>c/o Langley Research Center<br>Mail Stop 188A<br>Hampton, VA 23665-5225   | 1 |
| 6. LCDR Michael T. Coleman<br>Supervisor of Shipbuilding, Conversion<br>and Repair, U. S. NAVY<br>Pascagoula, Mississippi 39568-2210 | 3 |